

Precise and unbiased estimation of astigmatism and defocus in transmission electron microscopy

Miloš Vulović^{a,c,*}, Erik Franken^b, Raimond B.G. Ravelli^c, Lucas J. van Vliet^a, Bernd Rieger^{a,**}

^a Quantitative Imaging Group, Faculty of Applied Sciences, Delft University of Technology, Lorentzweg 1, 2628 CJ Delft, The Netherlands

^b FEI Company, Achtseweg Noord 5, 5651 GG Eindhoven, The Netherlands

^c Electron Microscopy Section, Molecular Cell Biology, Leiden University Medical Center, P.O. Box 9600, 2300 RC Leiden, The Netherlands

ARTICLE INFO

Article history:

Received 12 September 2011

Received in revised form

1 March 2012

Accepted 4 March 2012

Available online 12 March 2012

Keywords:

Transmission electron microscopy

Phase contrast

CTF

Twofold astigmatism

Defocus

Software

Thon rings

ABSTRACT

Defocus and twofold astigmatism are the key parameters governing the contrast transfer function (CTF) in transmission electron microscopy (TEM) of weak phase objects. We present a new algorithm to estimate these aberrations and the associated uncertainties. Tests show very good agreement between simulated and estimated defocus and astigmatism. We evaluate the reproducibility of the algorithm on experimental data by repeating measurements of an amorphous sample under identical imaging conditions and by analyzing the linearity of the stigmator response. By using a new Thon ring averaging method, the modulation depth of the rings in a 1D averaged power spectrum density (PSD) can be enhanced compared to elliptical averaging. This facilitates a better contrast transfer assessment in the presence of spherical aberration. Our algorithm for defocus and astigmatism estimation inverts the contrast of the Thon rings and suppresses the background in the PSD using an adaptive filtering strategy. Template matching with kernels of various ellipticities is applied to the filtered PSD after transformation into polar coordinates. Maxima in the resulting 3D parameter space provide multiple estimates of the long axis orientation, frequencies and apparent ellipticities of the rings. The frequencies of the detected rings, together with outlier rejection and assignment of an order to the CTF zeros, are used to estimate the defocus and its uncertainty. From estimations of defocus and ellipticity, we derive astigmatism and its uncertainty. A two-pass approach refines the astigmatism and defocus estimate by taking into account the influence of the known spherical aberration on the shape and frequencies of the rings. The implementation of the presented algorithm is freely available for non-commercial use.

© 2012 Elsevier B.V. All rights reserved.

1. Introduction

In order to improve resolution and allow reliable quantitative image analysis in transmission electron microscopy (TEM), it is essential to account for the effects of the oscillating contrast transfer function (CTF) on the image formation, the elastic and inelastic scattering properties of the sample, and the effects of the TEM detector. Determination of the CTF parameters, especially defocus and twofold astigmatism, is crucial in designing post-processing strategies to account for the effect of the CTF and for interpretation of the images at spatial frequencies beyond the first zero of the CTF. Additionally, in high resolution electron

microscopy (HREM), the unbiased and precise estimation of defocus and astigmatism forms the basis for the assessment of the maximal contrast transfer of the microscope, the optimal adjustment of aberration correctors, exit wave reconstruction, and the modeling of image formation.

Early descriptions of the influence of these aberrations on the CTF can be found in [1,2]. One of the most commonly used autofocus routines in TEM (especially for life-sciences) is based on a beam-tilt induced image displacement [3]. In order to obtain accurate estimates of defocus and astigmatism it is desirable to measure them from diffractograms of an amorphous sample, and avoid changes of the imaging conditions and possible introduction of higher order aberrations due to tilting of the beam. Many methods [4–20] base the CTF parameters estimation on the patterns in a diffractogram known as Thon rings [2] (see also Fig. 1B). The CTF parameters are usually estimated by minimizing the discrepancy between the background-subtracted power spectrum densities (PSD) of simulated and measured projections [4,7–9,11–15,18,20].

* Corresponding author at: Quantitative Imaging Group, Faculty of Applied Sciences, Delft University of Technology, Lorentzweg 1, 2628 CJ Delft, The Netherlands.

** Principal corresponding author.

E-mail addresses: milos.vulovic@gmail.com (M. Vulović), b.rieger@tudelft.nl (B. Rieger).

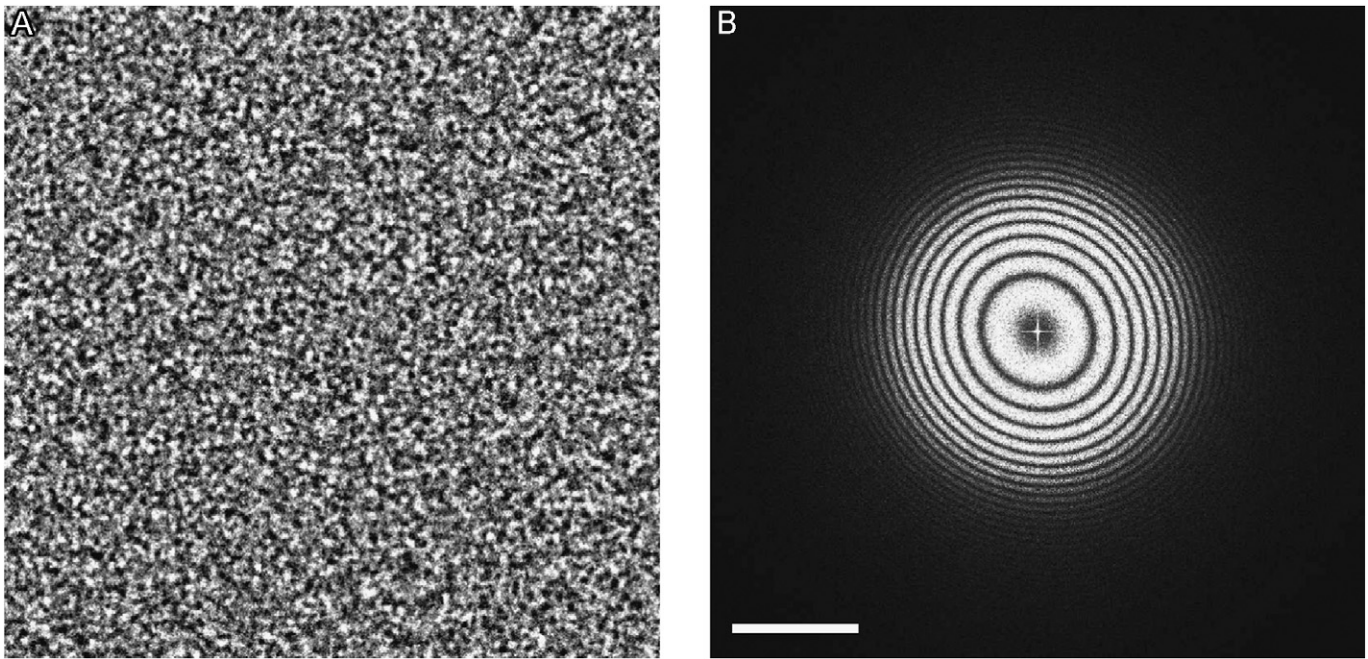


Fig. 1. (A) PTr sample imaged at a requested microscope underfocus of 1000 nm and magnification of 62 kx; (B) Power spectrum density (PSD) of the same image showing Thon rings that are not perfectly circular due to astigmatism. The scale bar corresponds to 0.5 nm^{-1} .

Some methods use 1D radial profiles obtained from circular averaging of 2D experimental PSD [4,8,11] or by elliptical averaging [17]. An inadequacy of circular averaging is that it neglects astigmatism. Astigmatism distorts the circular shape of the Thon rings and thus decreases their modulation depth in the obtained 1D profile. A few algorithms that consider astigmatism involve concepts such as dividing the PSD into sectors where Thon rings are approximated by circular arcs [15,21], applying Canny edge detection to find the rings [17] prior to elliptical averaging, determining the relationship between the 1D circular averages with and without astigmatism [22], or using a brute-force scan of a database containing precalculated patterns as in ATLAS [23]. Some other approaches for estimating CTF parameters do a fully 2D PSD optimization [12,14,18,20] but they usually regulate and fit numerous parameters by an extensive search that does not guarantee convergence. Furthermore, only a few schemes that were developed for defocus estimation provide an error analysis [23,24].

The background in the PSD hampers the Thon ring detection and therefore should be suppressed prior to estimation of defocus and astigmatism. The background dominates at low frequencies and originates from various contributions such as inelastic scattering, camera noise, and object structure. At high frequencies the oscillations are damped by the envelopes originating from the energy spread, finite source size, and the detector's modulation transfer function (MTF); as a result they submerge in the noise. Most state-of-the-art algorithms for defocus determination mentioned above [8–10,13–15,17] base their estimation on procedures that calculate a 1D averaged PSD, fit a non-linear background model through the PSD minima, and finally subtract it in order to extract the CTF oscillations. Background fitting, however, is a difficult step and often introduces systematic errors as no true model for background can be generated and the fitting is sensitive to the shape and the frequency range of the fitted model function. In [25] we analyzed the robustness of an approach based on background subtraction by characterizing the defocus estimation from each CTF zero individually. The minima at low frequencies were less reliable since they depend strongly on background subtraction. Hence, it is desirable to avoid fitting of a background function through the local PSD minima.

The precision of quantitative HREM image analysis is often limited by the precision of the related aberration estimations. The latest instrumentation improvements of aberration correctors require high precision and low bias of aberration estimates. For determination of higher-order aberrations, the Zemlin-tableau method [26] is commonly used which relies on accurate measurements of lower-order aberrations and requires acquisition of a number of images. In HREM, some of the alternative methods to Thon ring pattern recognition include estimation of defocus and astigmatism from crystalline regions [27] or using defocus series [28]. A number of algorithms developed for materials science applications report small absolute errors in defocus and astigmatism [23,27–31]. However, none of these algorithms consider estimation of small astigmatism (few nm) at high defocus values (order of a few microns) which implies very small ellipticity of Thon rings. Such settings are common for life-sciences applications where phase contrast imaging is used mostly at significant defocus.

Most state-of-the-art algorithms mentioned above are sensitive to background estimation and subtraction, thresholding of the PSD, and involve numerous intermediate steps that must be optimized. Peaks in diffractograms from crystalline material, incomplete appearance of the rings in a certain direction as a result of astigmatism, temporal envelope and/or sample drift represent an additional challenge [23]. Furthermore, the presence of spherical aberration (C_s) changes the frequency and shape of individual Thon rings, such that they can be only in approximation considered as ellipses. Although elliptical averaging (e.g. [17]) of the PSD is an improvement over the commonly used circular averaging, none of the approaches so far have included the influence of C_s on the shape of the rings in the averaging procedure to get one-dimensional Thon ring profiles; this becomes more important for a relatively small ratio between defocus and spherical aberration terms in the aberration function.

This paper presents and validates an unbiased and precise algorithm to automatically estimate defocus and twofold astigmatism from diffractogram(s) of an amorphous sample together with the corresponding uncertainties. We assume that astigmatism is smaller than defocus, i.e. Thon rings are approximately elliptical. This requirement is typically met in life sciences

applications where defocus is in the micrometers range. The algorithm, however, can also be applied to a range of parameter settings typical for materials science as long as the defocus is larger than astigmatism. The algorithm has been implemented in DIPimage, a MATLAB toolbox for scientific image processing and analysis, and will be freely available for non-commercial use via email upon request (<http://www.diplib.org/add-ons>).

2. Theory

2.1. Phase contrast

In approximation, image formation of weakly scattering objects in TEM can be considered as a linear process. For non-tilted and thin specimens, the defocus is constant across the field of view and therefore, the CTF is space-invariant. Phase contrast occurs as a result of interference between the unscattered part of the electron exit wave function and the elastically scattered part from the specimen. The electron wave is further subject to a frequency dependent phase shift introduced by the microscope aberrations. If we consider spherical aberration, defocus and twofold astigmatism, the total aberration function is

$$\chi(q, \alpha) = \frac{2\pi}{\lambda} \left(\frac{1}{4} C_s \lambda^4 q^4 - \frac{1}{2} \Delta f(\alpha) \lambda^2 q^2 \right), \quad (1)$$

where q is the magnitude of the spatial frequency (q_x, q_y). The relativistic electron wavelength λ depends on the energy of the incident electrons. It is assumed that the spherical aberration C_s is known. The defocus at eucentric height is Δf . We use the convention that underfocus implies $\Delta f > 0$, as in [32]. Twofold astigmatism (A_1, α_1) describes the azimuthal variation of (de)focus $\Delta f(\alpha) = \Delta f - A_1 \cos(2(\alpha - \alpha_1))$. (2)

The same sign convention is applied to A_1 as to defocus ($A_1 > 0$ corresponds to underfocus, and $\text{sgn}(A_1) = \text{sgn}(\Delta f)$). Fig. 2 illustrates the change of sign of A_1 while altering between underfocus

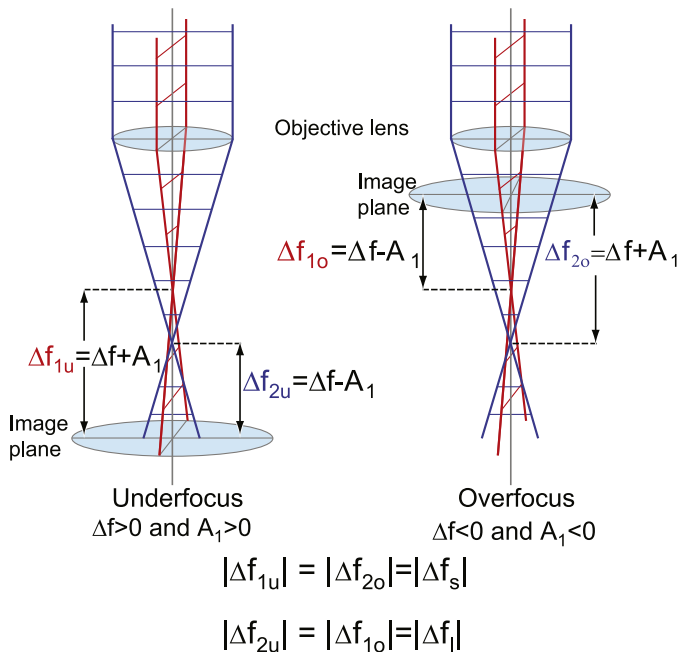


Fig. 2. Defocus and astigmatism follow the same sign convention $\Delta f > 0$, $A_1 > 0$ for underfocus and $\Delta f < 0$, $A_1 < 0$ for overfocus. Focal distances of tangential and meridional rays interchange while altering between underfocus and overfocus ($|\Delta f_{1u}| = |\Delta f_{20}|$ and $|\Delta f_{2u}| = |\Delta f_{10}|$). These defoci correspond respectively to the short q_s (Δf_s) and long q_l (Δf_l) axis of the Thon rings.

and overfocus due to the fact that the focal distances of the tangential and the meridional rays interchange. The transfer function of the lens system is [32]

$$T(q, \alpha) = e^{-i\chi(q, \alpha)}. \quad (3)$$

The Fourier transform ($\mathcal{F}[\circ]$) of the electron wave at the back focal plain is given by

$$\tilde{\Psi}(q, \alpha) = \mathcal{F}[e^{i\sigma v_z(x, y)}] T(q, \alpha), \quad (4)$$

where $v_z(x, y) = \int V(x, y, z) dz$ describes the projected scattering potential of the sample in z -direction of the incident electrons, $\sigma = \lambda me / (2\pi \hbar^2)$ is the interaction constant, and the tilde refers to the Fourier domain. Finally, the intensity in the image plane is defined as

$$I(x, y) = |\Psi(x, y)|^2. \quad (5)$$

2.2. Partial coherence and amplitude contrast

The energy spread and the finite source size introduce temporal and spatial incoherence respectively. These can be modeled as damping envelopes in the spatial frequency domain. The temporal incoherency of the source can be modeled as a chromatic envelope function K_c [32]:

$$K_c(q) = \exp \left[- \left(\frac{\pi \lambda q^2 C_c H}{4 \sqrt{\ln 2}} \right)^2 \right],$$

$$H \equiv \frac{\Delta E}{E}. \quad (6)$$

Here C_c is the chromatic aberration coefficient, which is usually of the same order of magnitude as C_s (a few mm). The energy of the incident electrons is E and the energy spread ΔE is around 1–2 eV for thermionic guns (LaB₆) and 0.3–0.5 eV for field-emission guns (FEG). See Table 1 for specifications used here. In the case of non-tilted illumination, K_c does not exhibit azimuthal dependency [33]. Furthermore, the finite source size introduces spatial incoherency which results in the spatial envelope:

$$K_s(q, \alpha) = \exp \left[- \frac{(\pi C_s \lambda^2 q^3 - \pi \Delta f(\alpha) q)^2 \alpha_i^2}{\ln 2} \right], \quad (7)$$

where α_i is the illumination aperture that is usually in the order of tenths or hundredths of mrad. The total incoherency of the source can be summarized as

$$K(q, \alpha) = K_s(q, \alpha) K_c(q, \alpha). \quad (8)$$

Furthermore, the thickness of the sample (t) induces another damping envelope [34]

$$K_t(q) = \text{sinc} \left(\frac{1}{2} \lambda q^2 t \right).$$

In our analysis, however, we assume that the influence of $K_t(q)$ is negligible compared to $K(q, \alpha)$. The influence of the objective aperture

Table 1
Some parameters and aberration constants of evaluated TEM microscopes.

Source	LaB ₆	FEG	X-FEG
V (kV)	120	200	300
ΔE (eV)	1.0	0.7	0.7
λ (pm)	3.35	2.51	1.97
C_s (mm)	6.3	2.0	2.7
C_c (mm)	5.0	2.0	2.7
α_i (mrad)	0.3	0.1	0.03

is described as

$$A_p(q) = \begin{cases} 1, & |q| \leq q_{\text{cut}}, \\ 0, & |q| > q_{\text{cut}}, \end{cases} \quad (9)$$

where $q_{\text{cut}} = 2\pi d_{\text{ap}}/(f\lambda)$ is the cut-off frequency, d_{ap} is the physical diameter of the aperture and f is the focal length of the objective lens. The amplitude contrast attenuation can be modeled by an imaginary term in the projected potential:

$$v_z(x,y) = V_z(x,y) + iA_z(x,y). \quad (10)$$

The amount of amplitude contrast is given by the ratio of the attenuation term to the magnitude of the projected potential:

$$W(q) = \frac{\tilde{A}_z(q)}{\sqrt{\tilde{A}_z(q)^2 + \tilde{V}_z(q)^2}}. \quad (11)$$

2.3. Weak-phase weak-amplitude object

In order to estimate the CTF parameters, the sample properties must be known. For that purpose the most convenient specimens are amorphous films. It is assumed that the overlap of atomic positions in a projection is significant and that the projected amorphous sample is essentially noise with a flat frequency spectrum. This is surely an approximation as every real specimen has limited scattering power. The mean inner potential of the sample introduces a constant phase change of the electron wave which can be neglected in this analysis as it is frequency independent. With these assumptions, the projected potential $v_z(x,y)$ is known and allows us to extract the CTF from the recorded image intensity. The total intensity for a weak-phase, weak-amplitude object is similarly as in [8,46] given by

$$I_0(x,y) = \mathcal{F}^{-1}[\delta(q) + \sigma \tilde{V}_z(q) \text{CTF}(q,\alpha)] \quad (12)$$

and the CTF is

$$\text{CTF}(q,\alpha) = 2A_p(q)K(q,\alpha) \sin(\chi(q,\alpha) - \Phi_a(q)) \quad (13)$$

where $\Phi_a(q) = \arcsin(W(q))$. We refer to Appendix A for detailed derivation of Eqs. (12) and (13).

2.4. Detector response

The measurement process yields Poisson noise, adds readout noise I_{rn} and integrated dark current I_{dc} to the final image, and blurs the image with a detector point spread function $\text{PSF}(x,y)$

$$I(x,y) = [CF \cdot N_{\text{pois}}(\Phi_e \cdot I_0(x,y))] * \text{PSF}(x,y) + I_{\text{rn}} + I_{\text{dc}}, \quad (14)$$

where $N_{\text{pois}}(A)$ denotes Poisson noise yield, CF is the conversion factor of the camera in $[ADU/e^-]$, $\Phi_e \cdot I_0(x,y)$ is the incident electron flux in $[e^-/\text{area}]$, and $*$ represents the 2D convolution operator.

2.5. Power spectrum density and ellipticity of Thon rings due to the astigmatism

The PSD of a mean-subtracted image is given by

$$P(q,\alpha) = |\mathcal{F}[I(x,y) - \langle I(x,y) \rangle_{x,y}]|^2, \quad (15)$$

where $\langle I \rangle_{x,y}$ denotes the mean intensity of the image. The minima in the PSD correspond to the zeros of Eq. (1). Fig. 1B displays the PSD of a recorded image of PtIr (platinum–iridium) showing a pattern referred to as Thon rings [2]. The observed contrast is minimal (Thon rings frequencies) when the CTF is zero. That occurs for zeros of the sine term in Eq. (13):

$$\chi(q,\alpha) - \Phi_a(q) = k\pi, \quad k \in \mathbb{Z}. \quad (16)$$

The location of a CTF zero depends on the defocus, the accelerating voltage, and the spherical aberration. By including the amplitude contrast into a so called effective k_{eff} we get

$$k_{\text{eff}} = k + \frac{\Phi_a}{\pi}. \quad (17)$$

For thin objects $k_{\text{eff}} \approx k$ usually holds, but we will keep k_{eff} for generality.

The shape of the Thon rings in the PSD is circular if no astigmatism is present. With increasing astigmatism (and $C_s \approx 0$) the shape gradually transits from elliptical to parabolic and hyperbolic. In the following, it is assumed that the astigmatism is not excessive such that the PSD contains near-elliptical equi-phase contours. The q^2 term in Eq. (1) has an azimuthal dependency ($\Delta f(\alpha)$), whereas the q^4 term with C_s is isotropic. This results in a shape of Thon ring which is not perfectly elliptical, especially for high frequencies. Let us for a moment consider the case without spherical aberration. The influence of C_s on the rings will be addressed later (see Section 3.6). In the case $C_s=0$, the rings are ellipses and the position of the CTF zeros can be found from:

$$\pi q^2 \lambda (-\Delta f + A_1 \cos(2(\alpha - \alpha_1))) = k_{\text{eff}} \pi. \quad (18)$$

From this expression we can find that the defocus in the direction of the long axis ($\alpha = \alpha_1$) of the Thon rings is given by

$$-\Delta f_l = \frac{k_{\text{eff}}}{\lambda q_l^2}, \quad (19a)$$

$$\text{with } \Delta f_l = \Delta f - A_1. \quad (19b)$$

Similarly, for the short axis ($\alpha = \alpha_1 \pm \pi/2$) we find

$$-\Delta f_s = \frac{k_{\text{eff}}}{\lambda q_s^2}, \quad (20a)$$

$$\text{with } \Delta f_s = \Delta f + A_1. \quad (20b)$$

The frequencies q_l and q_s represent the PSD minima in the long and short axis direction respectively; Δf_l and Δf_s are the corresponding defoci. It holds that $q_s < q_l$ and $|\Delta f_s| > |\Delta f_l|$. The ellipticity of a Thon ring is given by

$$R_0 = \sqrt{\frac{\Delta f_s}{\Delta f_l}} = \sqrt{\frac{\Delta f + A_1}{\Delta f - A_1}}, \quad R_0^2 \geq 1. \quad (21)$$

In the case $C_s=0$, the ellipticity represents the ratio between the long and short axes of the ellipse:

$$R_0 = \frac{q_l}{q_s}. \quad (22)$$

The twofold astigmatism is then derived from the defocus Δf and the ellipticity R_0 as

$$A_1 = \Delta f \frac{R_0^2 - 1}{R_0^2 + 1}. \quad (23)$$

3. The algorithm

An overview of the algorithm is shown in Fig. 3. In the first step, the PSD is obtained using Eq. (15). Then, the PSD contrast is inverted, the background suppressed, and the pattern denoised by an adaptive filtering procedure. Subsequently, in step 3 the PSD is resampled to polar coordinates. In this polar power spectrum image, Thon rings manifest themselves as straight lines when there is no astigmatism, or ‘sine-like’ curves when there is astigmatism present. The Thon rings can be found by probing the polar power spectrum image with templates (step 4) that resemble this expected Thon ring shape. This leads to a three-dimensional parameter space of frequency, orientation, and Thon ring ellipticity (step 5). In this space, the most dominant orientation

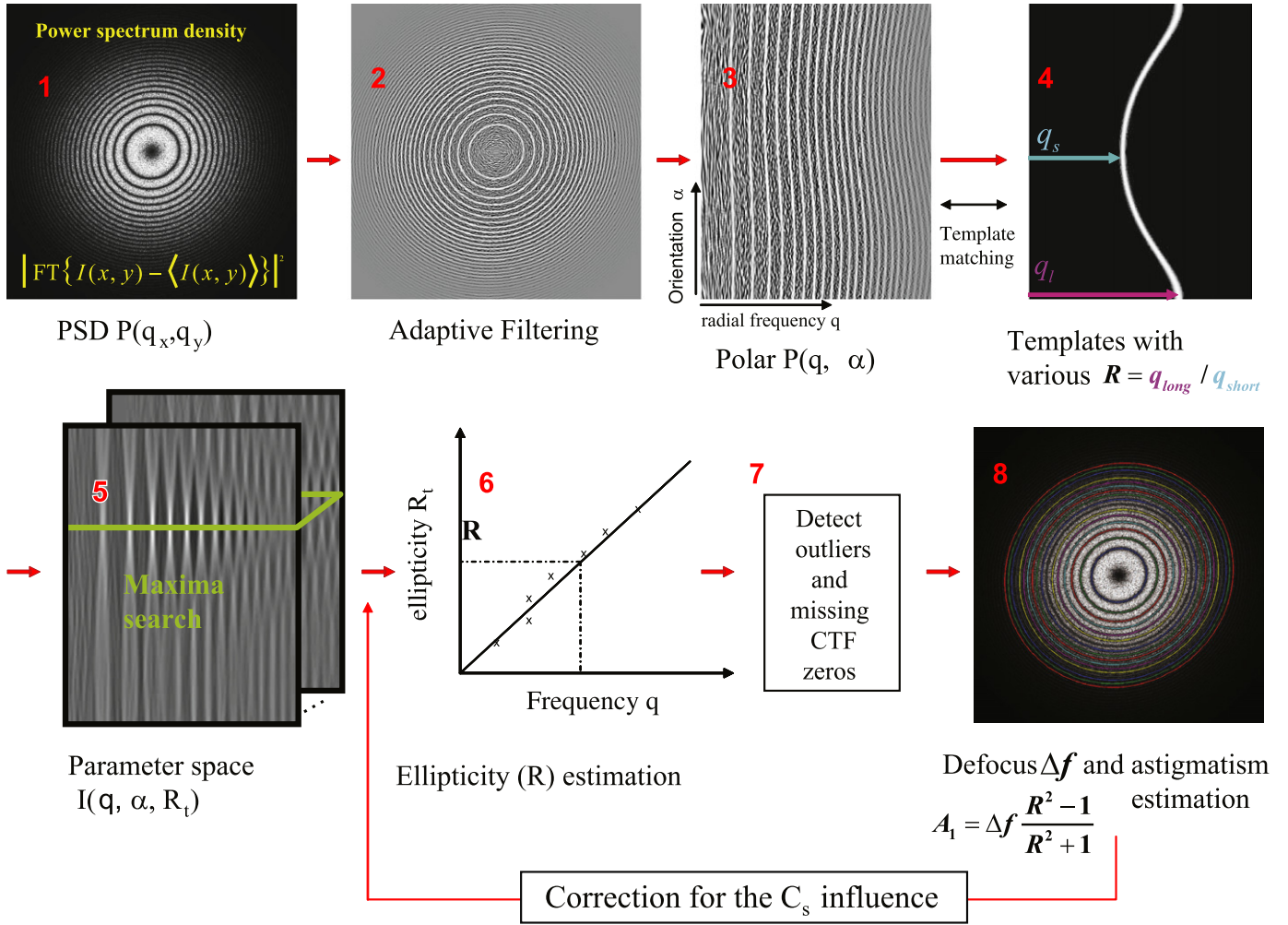


Fig. 3. Flow diagram of the algorithm. Note that we display the result after each step. Step 1, compute the PSD from an image; Step 2, suppress the background and invert the contrast of the rings by adaptive filtering; Step 3, transform from Cartesian into polar coordinates; Step 4, generate template and apply template matching; Step 5, find local maxima in parameter space; Step 6, find the ellipticity of the Thon rings; Step 7, detect outliers, identify missing CTF zeros, assign ordinal number to each CTF zero; Step 8, estimate defocus and astigmatism. Possible second pass for correction of the C_s influence.

and ellipticity of the Thon rings as well as their frequency are found by analyzing the local maxima. A model curve is fitted through the detected maxima peaks. The fit results in an estimate for the equivalent ellipticity R_0 , as defined in Eq. (21), which corresponds to the apparent ellipticity at the frequency of generated templates (step 6). Using the frequency of the found rings and by incorporating mechanisms (step 7) to remove outliers (false positives) and being able to deal with missing Thon rings (false negatives), the defocus value can be estimated. From the defocus value and ellipticity, the astigmatism can finally be calculated (step 8) using Eq. (23). If the ratio between the defocus and spherical aberration terms in Eq. (1) is low, we use a two-step approach and refine the initial astigmatism and defocus estimates (steps 6–8).

The next subsections explain all steps in more detail.

3.1. Power spectrum density processing

The PSD in Eq. (15) is calculated using a fast Fourier transform (FFT). In order to avoid possible edge effects, a Hann window can be applied to the image prior to PSD calculation. Spatial or frequency rebinning could be used to speed up subsequent calculations.

3.1.1. Periodogram averaging

There are different ways to improve the signal-to-noise ratio (SNR) of the PSD. These include periodogram averaging [7,8,12], averaging the PSDs of images of individual particles [4,11], additional angular averaging of the periodogram [4,7,8,11], classification and averaging of the PSDs of different micrographs [5,13], PSD enhancement [18,35] and parametric PSD estimation technique using autoregressive modeling [7] or 2D-autoregressive moving average modeling [14]. For images that have such a low SNR that the rings are barely visible, we chose to perform periodogram averaging. Patches with a fraction of the size of the original image ($N_{\text{patch}} = N/j$) ($j \in \{2, 4, 8\}$) of an untilted sample are selected, and multiplied by a Hann (cosine) window in order to avoid edge effects, i.e.

$$I_i(x, y) = I(x + a_{x,i}, y + a_{y,i})w(x, y), \quad (24)$$

where $w(x, y)$ is the Hann window, $x, y \in [1, N_{\text{patch}}]$, and $a_{x,i}, a_{y,i} \in [0, N - N_{\text{patch}}]$. Note that $a_{x,i}, a_{y,i}$ are the offsets for the entire patch i . The periodogram averaged PSD is defined as

$$P(q, \alpha) = \frac{1}{n} \sum_{i=1}^n P_i(q, \alpha), \quad (25)$$

where n is the number of patches and P_i is PSD of image I_i .

3.1.2. Background suppression

The background is suppressed and the contrast of the Thon rings is inverted using an adaptive filtering strategy. First, the logarithm of the PSD image is calculated which decreases the influence of the background slope. It also reduces the modulation depth variation of different rings. In this way, the widths of the Thon rings become more similar, and consequently, it is easier to detect them with a constant-width template.

An orientation-adaptive, second order Gaussian derivative filter [36] is applied to suppress the background and invert the contrast. Within the local footprint of the second order Gaussian derivative filter, the background is approximately linear and therefore suppressed. This adaptive filter assumes that the image is locally translation invariant along exactly one orientation (valid for line-like structures). As this is approximately true for all of the curved Thon rings which are straight within the filter's footprint, no disturbing artifacts are produced. As expected, we only perceive a slight compression of the contrast for the inner Thon rings. The method is in particular valuable for the dim outer Thon rings that obey the translation invariance to a very large extent. The filter kernel is anisotropic and smooths more along line-like structures such as the Thon rings than perpendicular to it. Furthermore, the spatial blurring of the adaptive filter could be modified to make the rings more prominent. The structure tensor [37,38] is used to estimate the local orientation which steers the adaptive filter [39,40]. The structure tensor was computed using a gradient scale of 1 and tensor scale of 20 pixels. These values proved to be robust against varying imaging conditions. Only in case of very small astigmatism, it is sensible, however, to avoid orientation estimation at all and assume a perfectly circular pattern. Any shifts between locations of the original Thon rings and the filter responses are corrected using the PLUS filter [41] as second derivative filter. Step 2 in Fig. 3 displays the PSD after applying this adaptive filtering.

3.2. Polar representation

The filtered PSD image is transformed into polar coordinates using cubic interpolation (step 3 in Fig. 3). This results in an image with one dimension (vertical in our display convention) representing angles (from 0 to π) and the other dimension representing frequency (horizontally from 0 to $N/2$, where N is the image size). Representing the angle α over an interval of π instead of 2π is possible since the PSD has Friedel's symmetry. The canonical implicit form of an ellipse whose long axis coincides with the q_x axis in Cartesian coordinates is given by

$$\frac{q_x^2}{q_l^2} + \frac{q_y^2}{q_s^2} = 1.$$

By substituting $q_x = q \cos \alpha$ and $q_y = q \sin \alpha$ and solving for q , an elliptical Thon ring in polar coordinates can be represented by

$$C(\alpha) = \frac{q_l q_s}{\sqrt{(q_s \cos(\alpha - \alpha_1))^2 + (q_l \sin(\alpha - \alpha_1))^2}}, \quad \alpha \in [0, \pi) \quad (26)$$

where α_1 is the angle between the long axis of the ellipse and the q_x axis. Step 3 in Fig. 3 suggests that the apparent curvature of the transformed rings (i.e. peak-to-peak amplitude) increases with frequency; however, all curves, when C_s is ignored, still have the same ellipticity q_l/q_s . It might be beneficial, although not necessary, to exclude the first few percent of the frequency range from the analysis where the original PSD was affected the most by the strong inelastic background.

3.3. Template generation and template matching

Template matching is performed by convolving templates of the shape of Eq. (26) with the polar image. The general approach would be to use the Radon transform. However, since in our case the shape of the template parameters are kept fixed, and only the position parameter is varied, the Radon transform can be implemented as a convolution [42,43].

3.3.1. Template generation

Generated templates consist of ellipses in polar representation which all have a zero angle orientation of the long axis ($\alpha_1 = 0$) and a "central frequency" (q_c) in the middle of the frequency range (at half Nyquist $N/4$, where N is the image size). We need to know this central frequency q_c of the Thon ring when aiming at estimating defocus. This is the frequency of the equivalent Thon ring without astigmatism, but with the same defocus. For the case that $C_s = 0$, we define, similarly to Eqs. (19a) and (20a):

$$q_c^2 = \frac{k_{\text{eff}}}{\lambda \Delta f}. \quad (27)$$

Using Eqs. (19b) and (20b) we observe the following relations for the short and long axis of a Thon ring:

$$\Delta f = \frac{1}{2}(\Delta f_l + \Delta f_s), \quad (28)$$

$$\frac{k_{\text{eff}}}{\lambda q_c^2} = \frac{1}{2} \left(\frac{k_{\text{eff}}}{\lambda q_l^2} + \frac{k_{\text{eff}}}{\lambda q_s^2} \right). \quad (29)$$

Solving the latter equations for q_c yields

$$q_c = \frac{\sqrt{2} q_l q_s}{\sqrt{q_l^2 + q_s^2}}. \quad (30)$$

The only parameter for the generated templates that is varied is the template ellipticity R_t which ranges from 1 to R_{max} with increments of dR . There is a need for a good compromise between template matching computation speed and precision. However, it is not crucial to know the exact value of R_{max} for template generation. The user could specify either the value for R_{max} directly or the uncertainty margins of the detected astigmatism. Given a specific uncertainty of the astigmatism estimation (e.g. 10%), we can combine the expected maximal astigmatism and given defocus value from the microscope to derive a rough estimate for R_{max} . A realistic approach is to predict the maximal number of detected CTF zeros ($N_{0 \text{ max}}$) from the pixel size and requested defocus value. Then we have $dR = (R_{\text{max}} - 1)/(2N_{0 \text{ max}})$. It is always possible to perform an estimation of R_{max} with one additional iteration. Initially, templates are generated with a large R_{max} and coarse dR to get a rough estimate of the astigmatism, and then use R_{max} estimated by equation Eq. (B.3) in B.1 for the second iteration. We used a fixed number of 100 templates (as default) ranging from 1 to R_{max} . Making dR smaller did not further improve the accuracy.

3.3.2. Search for maxima in the parameter space

After convolution of the templates with the polar image, the resulting parameter space image has three dimensions (frequency q , azimuthal angle α , and template ellipticity R_t). Maxima in the parameter space are found by watershed-based segmentation on the inverted parameter space image. The lowest values in the watershed segmented regions are the local minima and the minimal height difference between peak and valley is 20%. Sub-pixel localization is achieved by quadratic fitting through three points in each dimension at the same time. Each maximum provides the orientation of the long axis α_1 , frequency q_i and apparent ellipticity $R_{t,i}$ for Thon ring i . We construct a histogram

of the total weight of the found maxima with respect to azimuthal angle. The global mode in this histogram renders the angle of the long axis, since the angle of the long axis is common to all rings. Now the α coordinate is fixed, and a search for the maxima is performed again in the (q, R_t) -plane. In this way, the robustness of the algorithm is increased by imposing the constraint that all the rings must have an identical orientation of the long axis.

3.3.3. Zero astigmatism

If no astigmatism is present, the maxima in parameter space will be randomly placed along the long-axis orientation. Whatever value of the long-axis is selected has no influence on the estimated defocus value. Furthermore, the highest responses will be in the first plane ($R_{t,i} = 1$ for all rings i) of the three dimensional parameter space. In order to identify these responses as maxima, the watershed algorithm requires intensity comparison with neighboring pixels. For the responses that are at the edge of the parameter space we always expand the volume in the direction of $R < 1$ ellipticity. This is done by mirroring the first few slices in R direction at the plane $R = 1$, and then shifting them in α orientation direction by $\pi/2$ (now q_l becomes q_s and vice versa). Search for the maxima is performed only within $R \geq 1$. An additional control is performed by analyzing the slope of the responses in the (R, q) -plane. If the slope is smaller than 10^{-6} (which corresponds roughly to astigmatism less than 0.1 \AA per 1000 nm defocus), we assume that the responses are distributed at $R = 1$.

If no maxima are detected, the astigmatism will be ignored. All responses are projected in the direction of the angle and in the direction of the apparent ellipticity resulting in a reduced (one dimensional) parameter space where frequency q is the only remaining dimension. Maxima in this space represent frequency positions of the rings which are used to estimate only defocus, via the k -trajectory method (see Section 3.5). A similar approach (by reducing the parameter space from three to one dimensions) can be used for small astigmatism values to find defocus independently from the ellipticities.

If one is only interested in defocus estimation, the background-suppressed 2D PSD (Section 3.1.2) is initially angularly averaged and the frequency positions of the rings are found by searching the maxima in the 1D spectrum in a similar manner as described in Section 3.3.2. The angular averaging could be performed either in a non-weighted or a weighted manner. Weighted angular averaging is performed by computing the weighted average inside rings with a Gaussian profile to avoid problems arising from averaging too few data points at low spatial frequencies (see [44] for details). Weighted averaging, however, requires longer computational time. Note that by ignoring evident astigmatism, defocus estimation could be compromised as the SNR of the 1D angularly averaged spectrum decreases.

3.3.4. Correction for the difference between detected and template frequency positions

The radial frequency of a detected maximum does not reflect the true q_c of the Thon ring due to the difference between the mean values of the polar transformed PSD elliptical curve and that of the template generated elliptical curve Eq. (26). The mean value is the solution of an incomplete elliptical integral of the first kind (see Appendix B.2 and Eq. (B.6)) which depends on R_t . Each detected q has its corresponding R_t which is used to solve Eq. (B.6) numerically. In Appendix B.2 we derive the relative error between the detected q values of the maxima and the expected central frequencies q_c cf. Eq. (30). This relative error depends only on the ellipticities R_t that are used to convert the detected q positions to

the corresponding central frequencies q_c (Eq. (B.11)) which are further to be used for defocus and astigmatism estimation.

3.3.5. Derivation of Thon ring ellipticity from template ellipticity

Given a certain amount of astigmatism, templates with low ellipticities will match to the low frequency rings, and templates with a higher ellipticity to the higher frequency rings. We derived an analytical relation which predicts the behavior of the template matching ellipticities as a function of frequency (see Appendix B.1). This model is fitted through the detected maxima pairs $(q_i, R_{t,i})$. The ellipticity R_0 (common to all rings assuming $C_s \approx 0$) is the apparent ellipticity at the location of the generated templates (i.e. the middle of the frequency range, $N/4$). Additionally, if the number of detected maxima is larger than five (by default) we use robust fitting as implemented in the statistics toolbox of MATLAB. We define the uncertainty of the ellipticity value σ_{R_0} as a confidence interval of one standard deviation in the non-linear regression.

3.4. Outlier rejection

If the number of detected maxima is larger than four (by default) we can perform outlier rejection and analyze the central frequencies in the squared frequency (q^2) domain. The minima of the CTF are equidistant in q^2 space (for $C_s = 0$). Using this knowledge we exclude the points that do not follow this pattern (i.e. outliers) and identify gaps in the sequence of detected rings. Next, an order is assigned to the CTF zeros which are the input for the k -trajectory method used for defocus estimation. We refer to Appendix C for detailed information about the outlier rejection.

3.5. Defocus and astigmatism estimation

After outlier rejection, identification of the missing or false CTF zeros, and assigning k -values to the detected Thon rings using k -trajectory method [25], the defocus is estimated. Fig. 4A shows the square of the frequency dependent sine term in Eq. (13) for various amounts of normalized defocus with the positions of the minima (red) and maxima (green) superimposed. The location of the CTF zeros from Eq. (16) can be used to solve for the defocus from each (ordered) individual zero i as

$$\Delta f_i = \frac{C_s \lambda^3 q_{c,i}^4 - 2k_{\text{eff},i}}{2\lambda q_{c,i}^2}, \quad (31)$$

where $i \in \mathbb{N}$ is the assigned ordinal number of CTF zero and $q_{c,i}$ is the central frequency of ring i . For simplicity and without loss of generality lets assume a pure weak-phase object; i.e. $k_{\text{eff}} = k$. Amplitude contrast is taken into account in the final implementation by keeping k_{eff} . The problem we now face is: which k_i corresponds to the frequency $q_{c,i}$? For convenience of the analysis we use normalized dimensionless frequency $q^* \equiv q C_s^{1/4} \lambda^{3/4}$ and defocus $\Delta f^* \equiv \Delta f (C_s \lambda)^{-1/2}$. In case of overfocus ($\Delta f^* < 0$) in Fig. 4A, the i -th zero-crossing corresponds to $k=i$. However, in case of underfocus ($\Delta f^* > 0$), in the first region $q_{c,i}^* = 1$ corresponds again to $k=0$, but $q_{c,i}^*$ ($i > 1$) corresponds to $k=i-1$. For a normalized underfocus larger than $2^{1/2}$, positive k values are encountered. We visually explain k -trajectories in Fig. 4B. For each k -sequence, the values of Δf_i can be calculated using Eq. (31). The k -sequence for which Δf_i has the smallest relative variance is assumed to be the correct one. The mean value of all Δf_i is the estimate of the actual defocus. $\Delta f_{\text{est}} = \Delta f \pm \sigma_{\Delta f}$ where $\sigma_{\Delta f}$ is the standard deviation of the best sequence. There exist situations, for a relatively small ratio between defocus and spherical aberration phase contribution, when minima in the squared CTF do not correspond to a zero crossing in the CTF. They might be falsely detected as zero

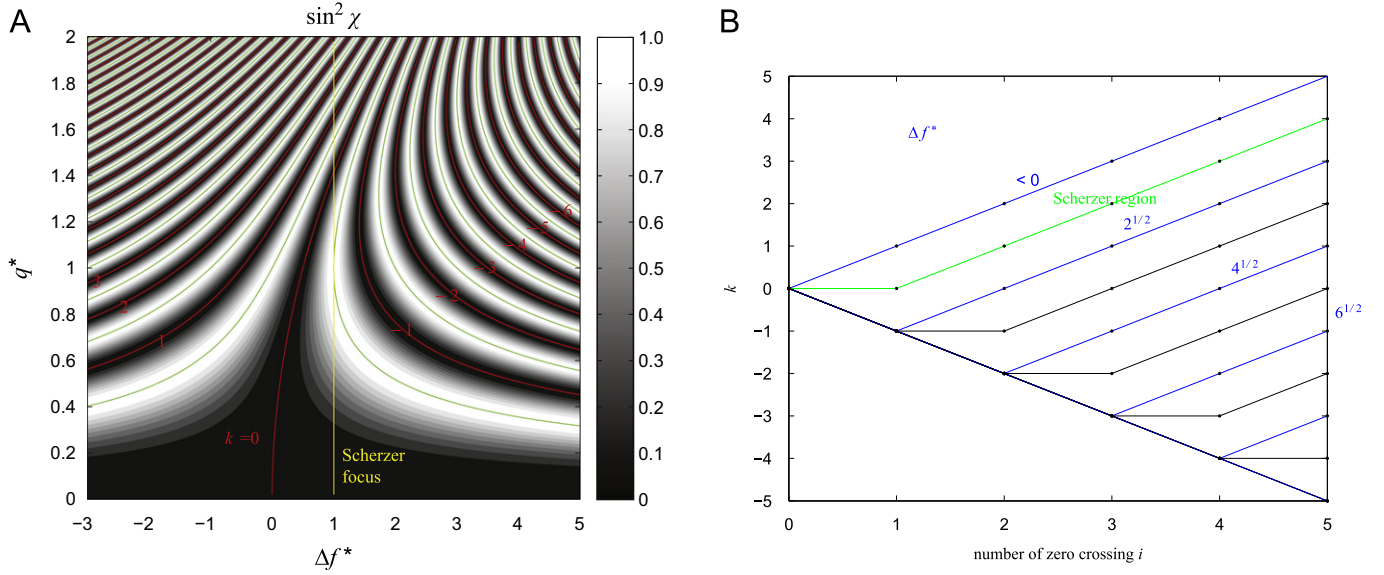


Fig. 4. (A) The square of the oscillating part of CTF in Eq. (13). The red and green lines indicate minima ($\sin^2(\chi(q))=0$) and maxima ($\sin^2(\chi(q))=1$) respectively. For simplicity and without loss of generality let us assume $k_{\text{eff}}=k$ (amplitude contrast is neglected). For convenience we use normalized dimensionless frequency $q^* \equiv qC_s^{1/4}\lambda^{3/4}$ and defocus $\Delta f^* \equiv \Delta f(C_s\lambda)^{-1/2}$. The Scherzer focus is represented by the yellow line. Following the q -axis direction, first a wide region of low contrast is encountered. In overfocus ($\Delta f^* < 0$) contrast improves, but the pass band is small and minima are quickly encountered. In underfocus ($\Delta f^* > 0$) there are regions where the maxima curves (green lines) are vertical. In those regions the contrast transfer is high for a wide frequency band. (B) The possible sequences of k -values for a certain zero crossing. In blue, the corresponding normalized defoci are indicated. In the vicinity of the Scherzer focus the k -sequence is equal to the green line. (For interpretation of the references to color in this figure legend, the reader is referred to the web version of this article.)

crossings, and could hamper the k -trajectory method. Therefore, we allow one of the local minima not to be a CTF zero (see [25]).

From defocus, ellipticity and their spreads we derive the astigmatism using Eq. (23). The standard deviation of the astigmatism is then

$$\begin{aligned} \sigma_{A_1} &= \sqrt{\left(\frac{\partial A_1}{\partial \Delta f} \sigma_{\Delta f}\right)^2 + \left(\frac{\partial A_1}{\partial R_0} \sigma_{R_0}\right)^2} \\ &= \sqrt{\left(\frac{R_0^2-1}{R_0^2+1} \sigma_{\Delta f}\right)^2 + \left(\frac{4\Delta f R_0}{R_0^2+1} \sigma_{R_0}\right)^2}, \end{aligned} \quad (32)$$

where σ_{R_0} is the standard deviation of the found ellipticity defined as one confidence interval of the fit (see Section 3.3.5).

3.6. Influence of spherical aberration C_s on the shape and frequency of Thon rings

The ratio between the spherical aberration and defocus terms in Eq. (1) is

$$\beta(q) = \frac{C_s \lambda^2 q^2}{2\Delta f}. \quad (33)$$

The presence of spherical aberration changes the positions of the high frequency Thon rings and in combination with astigmatism it might also change the ellipticity. This occurs for a relatively large value of $\beta(q)$ (e.g. > 0.2).

3.6.1. C_s influence on ellipticity

For non-zero C_s , the Thon rings do not have the same ellipticity. Therefore, we have to make a clear distinction in ellipticity of an individual Thon ring ellipse, which we will call Q_i for Thon ring i , given by

$$Q_i = \frac{q_{l,i}}{q_{s,i}} \quad (34)$$

and the earlier introduced dimensionless measure R_0 given by Eq. (21). Note that $Q_i|_{C_s=0} = R_0$ for all Thon rings.

The ellipticity with C_s for different Thon rings (k_i values) is given by (see Appendix D.1 for derivation)

$$Q_i(k) = \frac{|\Delta f_s| + \sqrt{\Delta f_s^2 + 2C_s k_i}}{|\Delta f_l| + \sqrt{\Delta f_l^2 + 2C_s k_i}} \quad (35)$$

Note that for underfocus negative k_i -values exist cf. Fig. 4. As shown in Fig. 5, ellipticity monotonically decreases with frequency in overfocus, while in underfocus ellipticity initially increases after which it decreases.

3.6.2. C_s influence on the frequency of the rings in q^2 -space

For outlier rejection, we use the property that the minima are equidistant in q^2 -space. However, the presence of C_s alters the frequencies of the Thon rings (see Appendix D.2 for details). Similar to the ellipticities, in overfocus the distances between neighboring minima become smaller while in underfocus the distances first increase and then decrease. Therefore, we derive a criterion for applying an additional iteration resulting in a two-step approach. In case that the relative error in equidistance between neighboring minima in q^2 -space (Eq. (D.9)) is larger than 25% (equally $\beta(q) > 10\%$), we decide to perform one additional iteration to correct for the C_s influence.

3.6.3. Correction for spherical aberration influence

From the parameter space of our template matching procedure as described in Appendix D.3, we can extract a value for Q_i for each Thon ring. However, for estimating the astigmatism, it is of interest to find the “equivalent ellipticity” $R_{\text{eq},i}$ when C_s would have been zero.

In D.3 we derive the “equivalent ellipticity” of a Thon ring as

$$R_{\text{eq}} = \sqrt{\frac{q_{l,i}^2(2\Delta f_l - C_s \lambda^2 q_{l,i}^2)}{q_{s,i}^2(2\Delta f_s - C_s \lambda^2 q_{s,i}^2)}} \quad (36)$$

Note, that the expression contains values for $\Delta f_s = \Delta f + A_1$ and $\Delta f_l = \Delta f - A_1$. This means that in order to calculate the equivalent ellipticity, one first needs to have an initial estimate of defocus

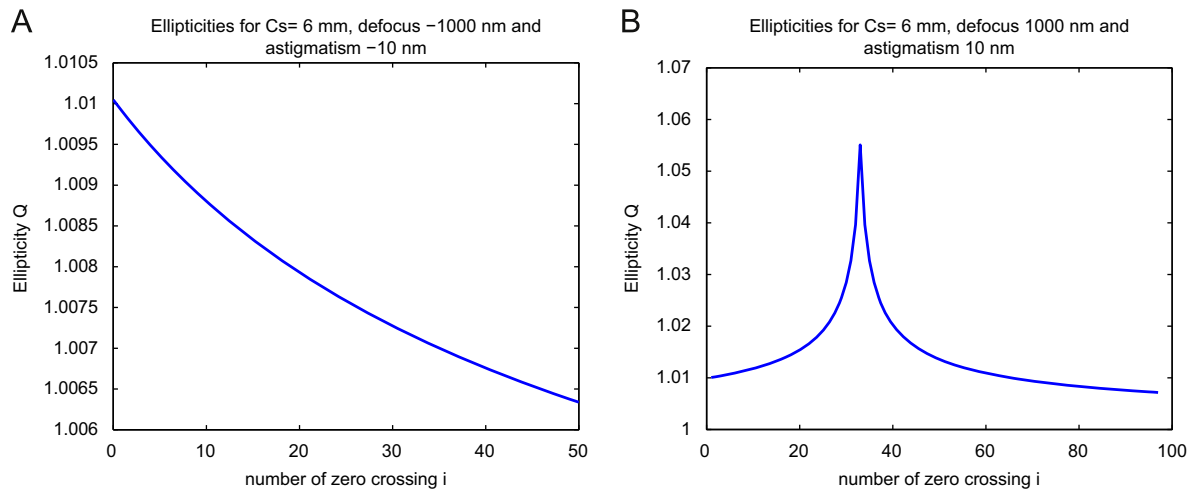


Fig. 5. The influence of the spherical aberration C_s on the Thon ring ellipticities. (A) In overfocus, ellipticity decreases monotonically with frequency. (B) In underfocus the ellipticity initially increases after which it decreases.

and astigmatism. Furthermore, in order to use outlier rejection it is desirable to know the C_s influence in Eq. (1) (i.e. β). Therefore, initially, we estimate the defocus from the first half of the PSD frequency range. The template matching function (Eq. (B.3)) is fitted to the frequencies for which $\beta < 0.1$. Now, using the estimated values, we estimate $R_{eq,i}$ using Eq. (36) and from that, the defocus and astigmatism.

4. Results

4.1. Validation by simulations

4.1.1. PSD simulations of an amorphous sample

Simulated images are obtained by taking into account effects of the specimen scattering properties, microscope aberrations, and camera characteristics (cf. Eq. (14)). The Fourier transform of the projected potential of a weak phase amorphous object is represented as:

$$\tilde{V}_z(q) = e^{i\varphi(q)} \quad (37)$$

where the amplitude of each frequency has the same constant value (equal to one) but the phase $\varphi(q)$ is random. Note that the phase distribution must be antisymmetric $\varphi(-q) = -\varphi(q)$ since the image is real. The Fourier transform of such a signal ($\tilde{V}_z(q)$) represents a white-noise object and its histogram is normally distributed with zero mean and standard deviation of one. The standard deviation of the generated $V_z(x,y)$ is normalized to 0.1 prior to applying the CTF and modulation transfer function of the camera (MTF). This normalization to 0.1 is necessary since Poisson noise can only be added to positive values; without the normalization, the inverse Fourier transform of the second term in Eq. (12) might become smaller than -1 , leading to negative intensity values. Furthermore, the normalization to 0.1 could be interpreted as phase-contrast initially set to 10% of the image intensity but further modulated by CTF and MTF. The MTF via edge method, conversion factors, readout noise, dark current noise of the cameras used for simulations were determined experimentally for different types of TEM cameras [44], and can be measured, including detective quantum efficiency (DQE) for any camera using online toolbox [44]. Table 1 gives the values for aberration coefficients and electron source incoherency used to simulate images for different types of microscopes. The PSD background is considered to originate mainly from inelastically scattered electrons and has been modeled as a Lorentzian radial distribution [45]. Although amplitude contrast $W(q)$ is usually

treated as a constant (~ 6 – 10%) [46], we allow a frequency dependency in the form of a Gaussian, as amplitude contrast is expected to give a larger contribution to the lower frequencies.

We simulated images with various values of defocus, various amounts and orientation of astigmatism, incident electron flux, and magnification for three different types of electron guns (LaB₆, FEG, and X-FEG), energies and TEM cameras. In order to check the reproducibility of the estimation, for each parameter combination, we simulated 60 different noise realizations. Since the astigmatism is known in the simulations, the R_{max} for template generation was predicted from Eq. (B.3) using the Nyquist frequency as q_c ; the number of generated templates was 100. Whenever necessary, in order to enhance SNR, rebinning in spatial or frequency domain is used.

4.1.2. Results from simulations

Precision and bias of defocus and astigmatism estimations are evaluated by simulations. Precision of the estimations as a function of astigmatism is shown in Fig. 6. Characterization of bias (absolute and/or relative error) of defocus and astigmatism estimations is presented in Table 2, Figs. 7–10. We observe a very good agreement between simulated and estimated defocus and astigmatism values. Given a particular magnification and camera size, defocus can be estimated with errors less than 4% for LaB₆ and 1% for X-FEG gun microscopes and with a small spread. Some examples from Table 2 include astigmatism values that range from 10 nm (LaB₆) down to 0.2 nm (X-FEG) with $\sim 10\%$ spread (for defoci of 1 and 2 μm). An example of a correction for the C_s influence on the ellipticity of the rings (see Section 3.6) is presented in Fig. 11.

Fig. 6 shows the uncertainty of the astigmatism, and statistical uncertainty (precision) of defocus, ellipticity, and astigmatism angle estimation for the X-FEG gun type microscope at a magnification of 200 k. The graphs show the precision represented by the standard deviation of the parameters estimation (+) as a function of astigmatism. For each defocus and astigmatism value, the estimation is characterized by its mean value and standard deviation. Each data point represents a series of 60 repeated measurements from which outliers were rejected. An estimation of defocus and ellipticity was considered to be an outlier (failure) if it differed more than three standard deviations from the median value of the set. The mean and standard deviation were recalculated without the outliers and concurrently the number of outliers is provided. The mean of the predicted astigmatism uncertainty values (\circ) in Fig. 6A was derived from the measured

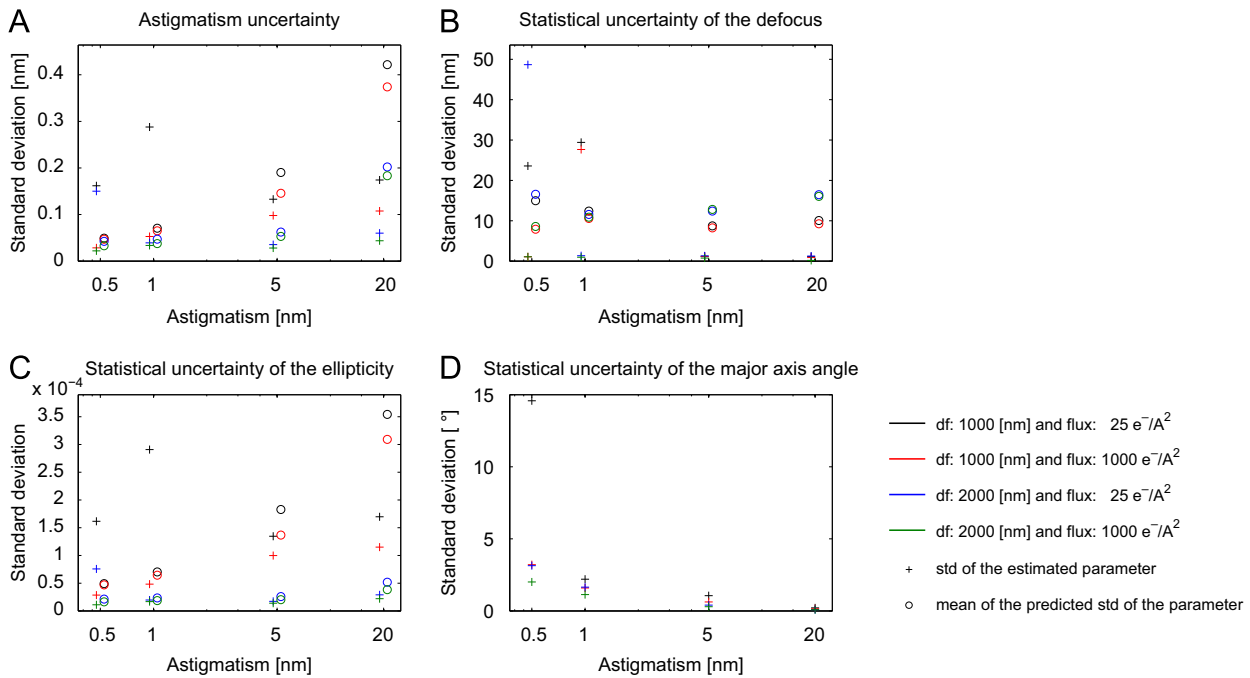


Fig. 6. Uncertainties of the estimated parameters for X-FEG gun type microscope at a magnification of 200 kx. Each data point represents a series of 60 repeated simulations from which outliers were rejected. The pluses (+) characterize the standard deviation (std) within the series of mean estimated values. The circles (o) characterize the mean of the predicted standard deviation of the estimation within the series. For better visibility pluses and circles are separated and shifted slightly to the left and to the right respectively from their real astigmatism values presented on the horizontal axis. (For interpretation of the references to color in this figure legend, the reader is referred to the web version of this article.)

Table 2

Results from simulations for three different types of the electron guns (LaB₆, FEG, and X-FEG) and TEM cameras [44]. For each parameter combination, 60 noise realizations were processed and the number of outliers (failures) is provided. An estimation of defocus and ellipticity was considered to be an outlier (failure) if it differed more than three standard deviations from the median value of the set. Mean absolute and relative errors of defocus and astigmatism are presented for two different electron fluxes: 25 and 1000 e⁻/Å².

Electron source	LaB ₆				FEG				X-FEG				X-FEG			
	2k × 2k		50 kx		2k × 2k		50 kx		2k × 2k		200 kx		4k × 4k			
Magnification	2–3				4–6				35–50				200 kx			
# of CTF zeros	2–3				4–6				35–50				72–80			
Defocus (nm)	1000		2000		1000		2000		1000		2000		2000			
Astigmatism (nm)	10		10		5		5		0.5		0.5		0.2			
Flux (e ⁻ /Å ²)	25	1000	25	1000	25	1000	25	1000	25	1000	25	1000	25	1000		
Defocus error	%	1.7	1.5	3.5	2.6	1.2	0.8	0.4	0.3	0.06	0.005	1.0	0.001	0.6	0.002	
	nm	17	15	70	52	12	7.6	8.2	5.0	0.60	0.05	20	0.20	12	0.04	
Astigmatism error	%	13	8.6	67	39	14	9.4	10	7.8	4.6	3.1	37	14	37	9.6	
	nm	1.3	0.9	6.7	3.9	0.7	0.5	0.4	0.02	0.02	0.02	0.07	0.1	0.07	0.02	
Relative error of ellipticity (%)	0.14		0.08		0.31		0.20		0.002		0.002		0.01		0.004	
# of outliers (out of 60 repeats)	0		0		2		2		1		0		4		2	

defocus and ellipticity uncertainties but also from their estimated values (Eq. (32)). The number of outliers is only 1–2 out of 60 for a high SNR. Fig. 6A–C shows astigmatism, defocus, and ellipticity uncertainties that are small compared to the absolute value. Furthermore, the spread (precision) of defocus and astigmatism estimations from repeated acquisitions (+) is often similar to the predicted uncertainty from one individual image (o). For astigmatism larger than 1 nm, Fig. 6A–C suggests that the estimated errors are smaller than the predicted errors. Estimations for higher fluxes (better SNR) generally perform better. Although the ellipticity for a fixed astigmatism is smaller for 2000 nm defocus than for 1000 nm, the results indicate that data for larger defocus give slightly better results than for lower defocus. This probably relates to the larger number of rings for higher defocus. Determination of the astigmatism angle is shown in Fig. 6D and indicates that the uncertainty rises with smaller astigmatism strength. This is expected as the peak detection in parameter space is compromised for very small ellipticity values.

Fig. 7 shows the mean of the absolute and relative errors of astigmatism estimation within a series of repeats. Depending on the values of defocus, astigmatism, and flux, the relative error varies from a few percent to a few tens of a percent. In general, the absolute value increases with astigmatism strength while the relative error decreases.

The mean absolute and relative error of defocus estimation are shown in Fig. 8. The horizontal axis now represents three different defoci, the different colors denote different fluxes and magnifications, while the mean errors of defocus are additionally averaged over four different values of astigmatism (the values on the horizontal axis in Fig. 7) since it is expected that defocus is independent of astigmatism. The estimation error is better than 1%. In a similar manner we characterized the errors of the ellipticity estimates (Fig. 9), that were used for the calculation of astigmatism via Eq. (23). The sensitivity of the estimator is high, being able to detect ellipticity down to 1.0004 with a relative error of only 10⁻³%.

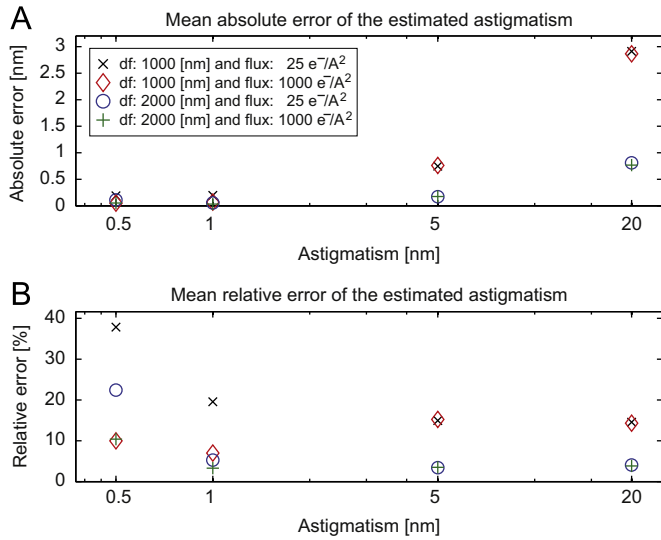


Fig. 7. Mean absolute (A) and mean relative (B) errors of estimated astigmatism as a function of the simulated astigmatism for X-FEG gun type microscope at a magnification of 200 kx (for two different defoci and fluxes). Each data point represents a series of 60 repeated simulations from which outliers were rejected.

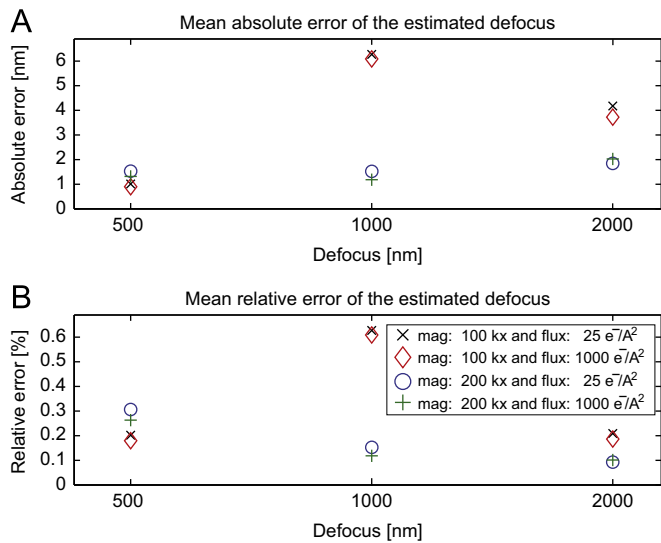


Fig. 8. Mean absolute (A) and mean relative (B) errors of estimated defocus as a function of simulated defocus for X-FEG gun type microscope. The error values were averaged over all astigmatism values presented in Fig. 7. For comparison two different fluxes and magnifications were presented. Each data point represents a series of 60 repeated simulations from which outliers were rejected.

(see Table 2). Fig. 10 demonstrates that errors in the estimated long axis orientation angle increase with smaller astigmatism which is in agreement with Fig. 6D. Along with the uncertainties of defocus and astigmatism estimation, Table 2 also indicates the mean number of outliers and the number of detected zeros (rings) for different fluxes, defoci, and astigmatism values.

The images with isotropic CTF (no astigmatism) were further simulated for a X-FEG type microscope and 2k × 2k camera size. The mean absolute errors of astigmatism were 0.04 nm and 0.08 nm for defoci of 1000 nm and 2000 nm respectively and for an electron flux of 25 e⁻⁷/Å².

4.2. Results from measurements

The reproducibility of the algorithm was evaluated using ten sequentially repeated measurements of a platinum–iridium (PtIr)

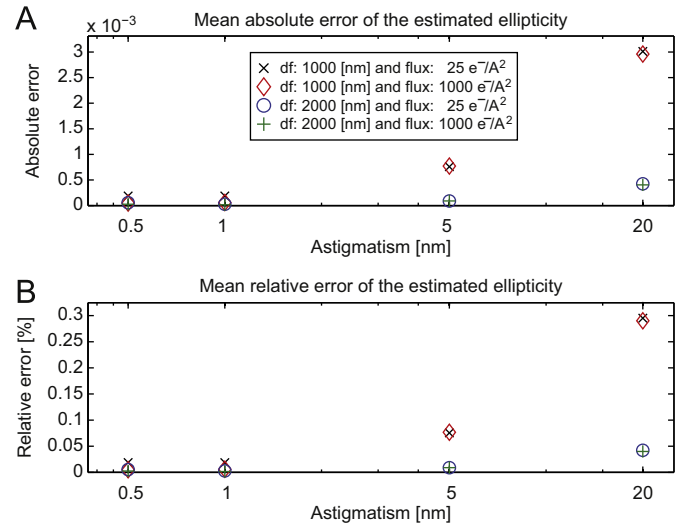


Fig. 9. Mean absolute (A) and mean relative (B) errors of estimated ellipticity as a function of simulated astigmatism for X-FEG gun type microscope at a magnification of 200 kx (for two different defoci and fluxes). Each data point represents a series of 60 repeated simulations from which outliers were rejected.

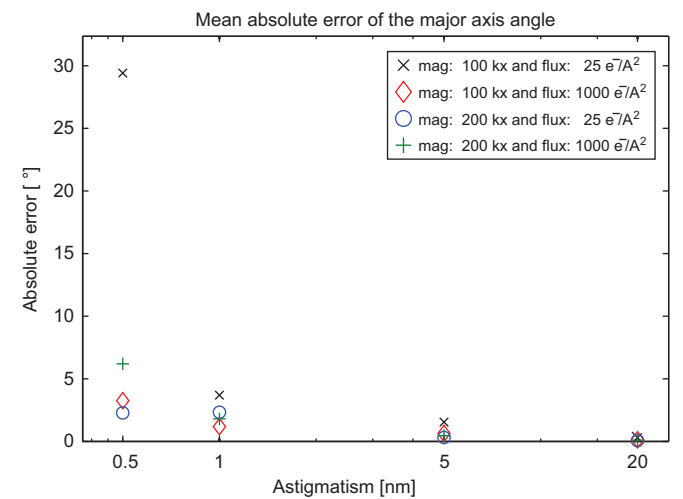


Fig. 10. Mean absolute errors of the long axis orientation as a function of simulated astigmatism for X-FEG gun type microscope at a magnification of 200 kx (for two different defoci and fluxes). Each data point represents a series of 60 repeated simulations from which outliers were rejected.

sample under identical conditions for different combinations of magnification, defocus and astigmatism. Unbinned images (4k × 4k) were collected on a Tecnai F20 (FEI Company, The Netherlands), using MATLAB scripts inspired by the TOM toolbox [47] and employing the TEMScripting ActiveX server. Series of images with four different stigmator settings were collected for three defocus values (500 nm, 1000 nm and 2000 nm). Three different magnifications (62 kx, 100 kx, 150 kx) were used. The incident beam was parallel and the incident electron flux was constant ($\approx 167 \text{ e}^-/\text{Å}^2$). Each series consists of ten repeated measurements under identical conditions. Whenever necessary, in order to enhance SNR, the rebinning or periodogram averaging was applied by using 20 patches of relatively large size $N_{\text{patch}} = N/2$ in order to maintain good sampling of high frequencies in the Fourier domain. Table 3 summarizes the results. The standard deviation of measured defocus and astigmatism within a series (+) is small and comparable to the mean value of the predicted standard deviations calculated from individual estimations (○).

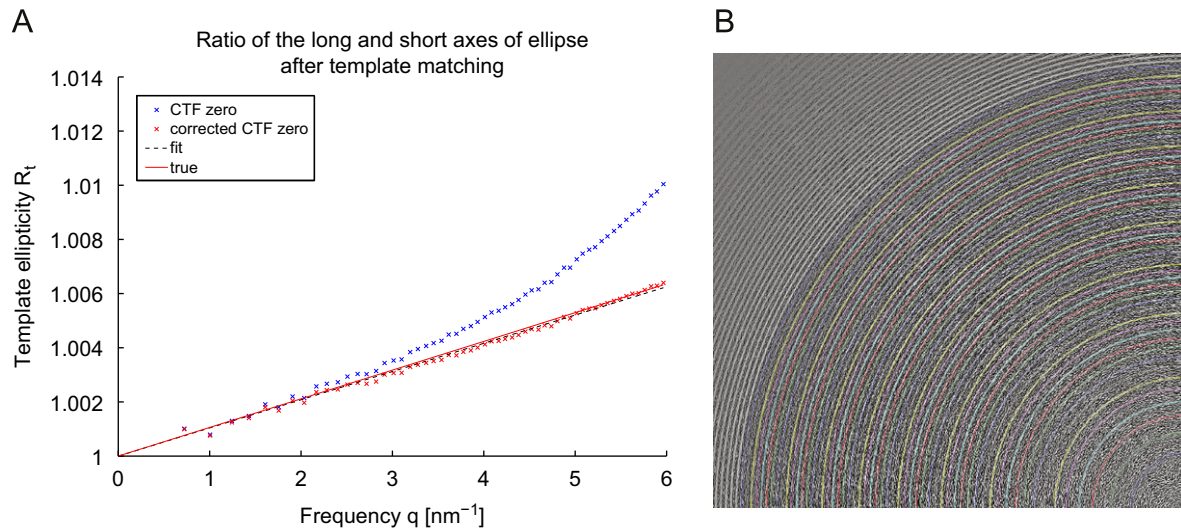


Fig. 11. (A) The apparent ellipticities of the rings after the template matching, with and without subsequent correction for the C_s influence (defocus 1000 nm, astigmatism 5 nm, $C_s = 2.7$ mm, magnification 200 kx, X-FEG source). (B) Overlay of positions and shapes of the found Thon rings with background suppressed PSD. (For interpretation of the references to color in this figure legend, the reader is referred to the web version of this article.)

Table 3
Robustness of the estimation evaluated on images of a PtIr sample acquired on a microscope with a FEG electron gun and $4k \times 4k$ camera. Series of images with four different stigmator settings were collected for three defocus values (500 nm, 1000 nm and 2000 nm). Three different magnifications of 62 kx, 100 kx, and 150 kx were used. The incident beam was parallel and the incident electron flux was constant ($\approx 167 \text{ e}^-/\text{\AA}^2$). Each series consists of ten subsequently repeated measurements under identical conditions. The standard deviation of measured defocus and astigmatism within a series (+) is small and comparable to the mean value of predicted standard deviations calculated from individual estimations (\circ).

Requested defocus (nm)	Error (nm)	Δf_{est}	ast ₁ (62 kx)		ast ₂ (62 kx)		ast ₃ (62 kx)		ast ₄ (62 kx)	
500	Measured +	561.8 ± 5.5	16.2 ± 6.6	12.9 ± 1.8	14.5 ± 2.7	11.5 ± 4.6				
	Predicted \circ		16.2 ± 1.9	12.9 ± 2.0	14.5 ± 2.4	11.5 ± 1.6				
1000	Measured +	1051 ± 5.7	22.5 ± 1.0	18.1 ± 1.3	15.4 ± 1.3	7.9 ± 1.5				
	Predicted \circ		22.5 ± 0.8	18.1 ± 0.8	15.4 ± 1.0	7.9 ± 1.2				
2000	Measured +	2050 ± 6.6	32.7 ± 1.3	28.1 ± 0.7	25.4 ± 1.1	6.3 ± 1.0				
	Predicted \circ		32.7 ± 1.0	28.1 ± 0.9	25.4 ± 0.8	6.3 ± 1.0				

			ast ₁ (100 kx)		ast ₂ (100 kx)		ast ₃ (100 kx)		ast ₄ (100 kx)	
500	Measured +	300.9 ± 6.6	19.0 ± 1.9	14.8 ± 4.3	12.9 ± 1.9	22.4 ± 5.8				
	Predicted \circ		19.0 ± 1.5	14.8 ± 1.6	12.9 ± 4.2	22.4 ± 2.5				
1000	Measured +	732.6 ± 5.0	18.8 ± 1.8	14.9 ± 3.9	13.7 ± 1.1	11.6 ± 5.0				
	Predicted \circ		18.8 ± 2.6	14.9 ± 2.5	13.7 ± 2.2	11.6 ± 2.2				
2000	Measured +	1724 ± 8.0	25.6 ± 1.0	20.2 ± 1.2	18.4 ± 1.5	12.8 ± 2.6				
	Predicted \circ		25.6 ± 1.0	20.2 ± 1.0	18.4 ± 0.9	12.8 ± 4.3				

			ast ₁ (150 kx)		ast ₂ (150 kx)		ast ₃ (150 kx)		ast ₄ (150 kx)	
500	Measured +	551.6 ± 5.9	18.8 ± 1.8	14.7 ± 1.8	12.0 ± 1.2	10.6 ± 3.6				
	Predicted \circ		18.8 ± 1.5	14.7 ± 1.4	12.0 ± 1.7	10.6 ± 1.6				
1000	Measured +	1030 ± 4.1	21.2 ± 1.3	16.5 ± 0.7	14.5 ± 0.5	6.5 ± 1.1				
	Predicted \circ		21.2 ± 0.7	16.5 ± 0.7	14.5 ± 0.7	6.5 ± 1.1				
2000	Measured +	1982 ± 5.6	30.6 ± 0.7	25.6 ± 0.8	24.0 ± 1.0	4.7 ± 1.3				
	Predicted \circ		30.6 ± 1.1	25.6 ± 1.0	24.0 ± 1.0	4.7 ± 0.7				

The linearity of the stigmator response was evaluated on data acquired using the same sample on a Titan microscope. The microscope was equipped with a Falcon CMOS direct electron detector and operated at 300 kV voltage. A series of images with increasing strength of the stigmatizers (x and y) in both directions (positive and negative) were collected. The results of the astigmatism estimation for 450 nm overfocus are shown in Fig. 12. The projections of astigmatism on the x - ($A_{1x} = A_1 \cos \alpha_1$) and y -axes ($A_{1y} = A_1 \sin \alpha_1$) were calculated. The linearity was assessed by making a linear least-squares fit to the estimated projected

astigmatism versus stigmator strength (see Fig. 12A). The square of the sample correlation coefficient between the measured and predicted values, within the range of measured astigmatism values, was nearly one: 0.9998 and 0.9997 for negative and positive y stigmator strengths respectively. Fig. 12B shows the relation between x and y projected astigmatism. Linear least-squares fits for all four data sets (increase and decrease of x and y stigmator strengths) were calculated. The angles between the introduced astigmatism were nearly 90° . This corresponds well to the expected orthogonality while altering between the positive

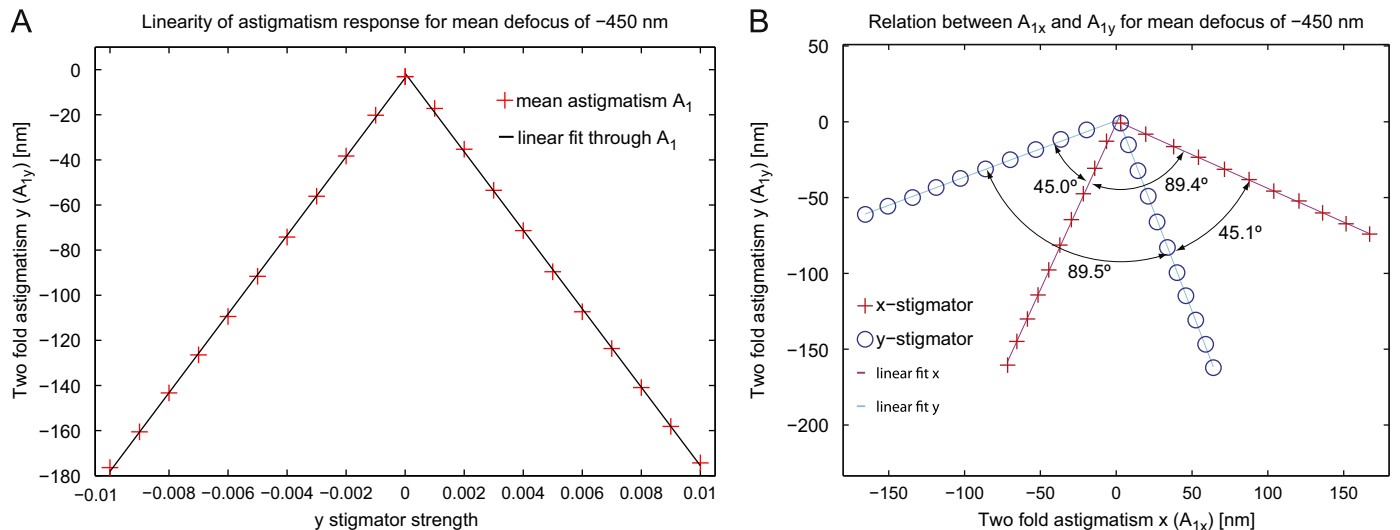


Fig. 12. The response of microscope's stigmators evaluated using a PtIr sample on a Titan microscope (at 300 kV and 250 kx magnification) equipped with a Falcon CMOS direct electron detector. Series of images with increasing strength of the stigmators (x and y) in both directions (positive and negative) were collected. The projections of astigmatism on the x ($A_{1x} = A_1 \cos \alpha_1$) and y axes ($A_{1y} = A_1 \sin \alpha_1$) were calculated. (A) Linearity of estimated y -projected astigmatism A_{1y} versus y stigmator strength for 450 nm overfocus. The linearity was validated by high coefficient of determination: 0.9998 and 0.9997 for negative and positive y stigmator strengths respectively. Additionally, the slopes of the lines show good agreement (-17.44 and 17.39). (B) Relation between x - and y -projected astigmatism values. The angles between x - and y -projected astigmatism values were nearly 90° . The angles between cyan–magenta lines were close to 45° and correspond well to the final orthogonality between x and y stigmators. Equidistant data points within a series indicate linearity, already presented in (A). (For interpretation of the references to color in this figure legend, the reader is referred to the web version of this article.)

and negative values of a stigmator. The introduced astigmatism changes with twice this angle (Eq. (2)). For the same reason, the angles between lines of the x and y stigmator were close to 45° correspond well to the orthogonality between x and y stigmators. Equidistant data points within a series indicate linearity, already presented in Fig. 12A.

4.3. Thon ring assessment

In this section we will evaluate our CTF estimation algorithm as a tool for assessing Thon rings. In particular the modulation depth of the rings as a measure for useful contrast transfer as a function of spatial frequency. For this purpose, we first analyze the performance of our Thon ring averaging method, as this is an important prerequisite to objectively assess the Thon rings from 1D CTF profiles. Subsequently, we will introduce a quantitative measure for Thon ring visibility and show some results on real images.

4.3.1. Thon ring averaging

The algorithm for Thon ring averaging (TRA) is described in Appendix E. Our new TRA method extends the elliptical averaging method by taking into account C_s influence on the ellipticity of the rings. Fig. 13 illustrates the difference between circular, elliptical, and Thon ring averaging. For a certain combination of imaging parameters such as a large ratio β between the spherical aberration and defocus terms in Eq. (1), Thon ring averaging is advantageous to get a higher SNR of 1D PSD profiles.

4.3.2. A Thon ring visibility criterion

Defocus and astigmatism estimation is useful for assessing Thon rings and information transfer. That is, we want to quantify the contrast transfer of a TEM by Thon rings with regard to some criterion. For this purpose, we first accurately estimate the defocus and astigmatism, including the correction for the C_s effect (see Section 3.6). Subsequently, we calculate the Thon ring average as described in Appendix E and the theoretical positions of the maxima m_i and minima t_i (i.e. the Thon ring frequencies) in the angular average. The

modulation of the amplitude of the Thon ring i is then given by

$$M_i = \frac{\text{PSD}_{1D}(m_{i-1}) + \text{PSD}_{1D}(m_i) - \text{PSD}_{1D}(t_i)}{2}, \quad (38)$$

where m_{i-1} and m_i are the two closest maxima with $m_{i-1} < t_i < m_i$. The modulation depth of a Thon ring is defined as M_i/nf , where nf is the noise floor, found by calculating the average of the power spectrum that is outside of the Nyquist bound

$$nf = \frac{\sum_{|q| > N/2} \text{PSD}(q)}{\sum_{|q| > N/2} 1}. \quad (39)$$

A Thon ring is considered to be detected if its modulation depth is larger than two. Fig. 13 shows an example of the Thon ring assessment procedure.

5. Discussion and conclusions

Unbiased and precise defocus and astigmatism determination is necessary for CTF estimation and correction, assessment of microscope contrast, image modeling, optimal adjustment of aberration correctors, and exit wave reconstruction. It is also beneficial for the calculation of resolution metrics such as Fourier ring correlation [48]. We have presented an algorithm for the unbiased and precise estimation of defocus and astigmatism from the PSD of TEM images of amorphous specimens. The algorithm provides an error estimate and automatically rejects outliers. Tests show very good agreement between simulated and estimated values of defocus and astigmatism (Table 2). Given a particular magnification and camera size, defocus can be estimated with a small spread and errors less than 4% for LaB₆ and 1% for X-FEG gun microscopes. Some examples include astigmatism values that range from 10 nm (LaB₆) down to 0.2 nm (X-FEG) with a $\sim 10\%$ spread (for defoci of 1 and 2 μm). We chose relatively large defocus values, typical for life sciences, to demonstrate the ability to detect small astigmatism (very small ellipticity). We evaluated the reproducibility of the algorithm on experimental data by repeating measurements under identical TEM imaging

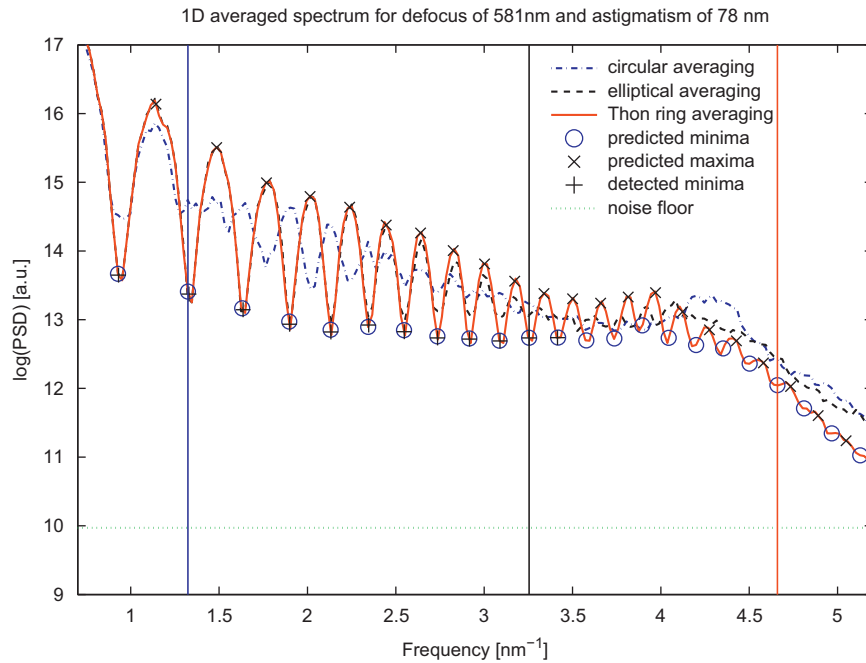


Fig. 13. Thon ring averaging and Thon ring assessment. Thon ring averaging (TRA), elliptical and circular averaging methods are compared. The horizontal axis represents the central frequency q_c given by Eq. (E.4). TRA is advantageous when C_s influence on the ellipticity of the rings is not negligible. The image of PtIr sample was acquired with a Titan microscope (at 300 kV and 380 k magnification) equipped with a Falcon CMOS direct electron detector and FEG electron gun. Estimated defocus 581.4 ± 0.5 nm; estimated astigmatism 78.2 ± 0.4 nm; spherical aberration 2.7 mm. Note that up to ~ 3 nm $^{-1}$ elliptical averaging and TRA are perfectly in phase, but they appear uncorrelated. Thon ring assessment: the green dotted horizontal line shows the estimated noise floor and the vertical lines show the result of the Thon ring assessment, i.e. modulation amplitude of the Thon ring is twice higher than the noise floor for all frequencies left of the vertical line. (For interpretation of the references to color in this figure legend, the reader is referred to the web version of this article.)

conditions for a few defocus and astigmatism values (see Table 3). The autofocus routine (which works by measuring the beam-tilt induced image displacement) of the microscope was executed before each magnification series and then moved to the requested defocus. The reason for the mismatch between requested and estimated defocus at the magnification of 100 k might be an inaccurate defocus calibration (i.e. the calibration that relates beam-tilt induced image shift to defocus values) for this particular magnification. Our approach requires that the sample is amorphous or near-amorphous. Both amorphous carbon and PtIr satisfy this requirement. Actually, for the PtIr sample, the grains of PtIr are evaporated on carbon film. The advantages of PtIr is that this specimen may be used to test the resolution of the electron microscope by the point separation test, gives an intrinsic magnification calibration by the PtIr reflexion at ~ 2.35 Å and might scatter to higher frequencies than carbon. However, we do not use calibration properties in our evaluations (only amorphousness). The algorithm was used to analyze the response of the stigmators which was validated to be linear (Fig. 12). The uncertainty of the defocus estimation from one image depends on the number of detected zeros. As shown in Fig. 6 and Table 3, the spread of defocus and astigmatism estimations from repeated acquisitions is often similar to the predicted uncertainty from an individual image, although they inherently represent different statistical measures. Additionally, we show that accounting for the influence of astigmatism and C_s enhances the modulation depth of the 1D averaged PSD and helps assessing the quality of the contrast transfer.

The algorithm suppresses the background in the PSD using an adaptive filtering strategy that avoids the need for conventional estimation of the frequency range of the 1D background and fitting of a model through the PSD minima. Furthermore, an anisotropic background as mentioned in [18] can be addressed in this way. The method itself relies on template matching using

kernels of various ellipticities. Maxima in the 3D parameter template space provide the long axis orientation, frequencies and apparent ellipticities of the rings. From these parameters we derive an equivalent ellipticity (R_0), common to all rings, which corresponds to the apparent ellipticity at the position of the generated template.

The frequencies of detected Thon rings are used to estimate the amount of defocus via the k -trajectory method as described in [25]. This method assigns an integer number k to each detected Thon ring (CTF zero). Several defoci can be computed from the CTF zeros, but the value with minimal normalized standard deviation is taken as the final defocus estimate. Accuracy is hard to assess in the actual experiments since the true values are unknown. However, theory governs that the estimated defocus values for the different Thon rings should be consistent. Each defocus estimation based on more than one Thon ring is accompanied by the uncertainty $\sigma_{\Delta f}$ (see Section 3.5). If the provided C_s value, electron energy, measured magnification and the amount of amplitude contrast are correct, it is very unlikely that there exists a systematic disturbance which shifts the CTF zeros in such a way that $\sigma_{\Delta f}$ stays the same or decreases. This would be only possible if we falsely detect spurious CTF zeros at regular positions between every true CTF zero (including one before the first zero). Under all these assumptions, $\sigma_{\Delta f}$ can be used as a measure of accuracy which incorporates both bias and precision [49]. Additionally, it can be used as a sorting criterion, without having to evaluate repeated measurements.

Spurious or missed rings in the PSD are automatically identified and accounted for. This means that estimations can be done from any subset of rings, not relying exclusively on the first few minima in the PSD as is usually done. The outlier rejection and CTF zeros ordering use the fact that zeros of the CTF are equidistant in squared frequency space (for $C_s=0$). An additional control is performed in the k -trajectory method where one

possible false CTF zero that occurs for a small ratio between defocus and C_s phase terms is discarded. Furthermore, the k -trajectory method is capable of distinguishing between underfocus and overfocus (for $C_s \neq 0$ or amplitude contrast $W(q) \neq 0$).

Ignoring the influence of spherical aberration on the CTF results in a deviation of the apparent ellipticities from anticipated ones (blue crosses in Fig. 11) at high spatial frequencies and/or relatively low defocus values. We predict and correct for this C_s influence in a two-pass refining process (red crosses Fig. 11A) and accurately map the Thon rings (Fig. 11B). In addition, we introduce a new angular averaging method, Thon ring averaging (TRA), which takes into account the influence of C_s on the ellipticity of the rings; TRA averages over true Thon rings to get the 1D PSD, rather than averaging over circles or ellipses. TRA proves to be superior (Fig. 13) especially in cases when the ratio between the spherical aberration and defocus terms in Eq. (1) is relatively large (e.g. $\beta(q) > 0.5$ where $\beta(q)$ is defined in Eq. (33)). The Thon ring assessment as described in Section 4.3 uses TRA and is a useful tool for microscope contrast transfer assessment.

The typical processing time depends on the input image size and the accuracy required. Spatial or frequency rebinning could be used to speed up subsequent calculations. The default settings in the software are currently such that images are binned to 512×512 pixels after which the estimation takes a few seconds if the templates were pre-computed and stored on disk or half a minute if 50 templates have to be generated (on a computer running at 2.7 GHz with 4GB RAM). However, a high accuracy and detection of very small astigmatism requires computation time. Another advantage of rebinning is that it can enhance the SNR. Nevertheless, one should use rebinning with caution. For the PSD that has wider rings which also extend to high fraction of Nyquist frequency (e.g. relatively lower magnification and lower defocus), binning in the Fourier domain might be beneficial. If the PSD has rings that are narrow and close to each other, but they do not extend to a high fraction of Nyquist frequency (e.g. relatively high magnification and high defocus), spatial binning is beneficial.

In order to avoid possible edge effects, a Hann window can be applied to the image prior to PSD calculation. Here, the Hann window is only used for periodogram averaging. It is very wide (one period over the whole image) and is therefore very narrow in Fourier domain (effectively a kernel of only $\sim 3 \times 3$ pixels in the

Fourier spectrum). The convolution/blurring of the logarithm of the PSD is therefore small and a shift of the CTF zeros is expected to be sub-pixel and only measurable if there is a steep slope in the PSD to begin with.

Although the accuracy of the defocus value provided by the microscope software is seldom sufficient, this defocus value can still be used to assist in a rough initial estimation, in a prediction of the C_s influence, and in a prediction of the (equi)distance of minima in the squared frequency (q^2) space. Astigmatism distorts the circular shape of the PSD rings and decreases the SNR of the 1D PSD angular averages. We have assumed that astigmatism is not excessive (astigmatism is not larger than defocus) and the Thon rings are still approximately elliptical. These requirements are typical for life sciences applications where phase contrast imaging is used mostly at relatively high defocus. The algorithm, however, can also be applied to a range of parameter settings typical for materials science as long as the defocus is larger than astigmatism. Provided that the astigmatism is relatively large but not excessive it is possible to extract the astigmatism even from the circularly averaged PSD [22]. Our algorithm, however, is able to detect very small astigmatism as well.

Although there are numerous aberrations in TEM, we focus here on robust and unbiased determination of defocus and astigmatism as they are crucial for the measurements based on diffractogram tableaux of all higher-order aberrations such as coma and threefold astigmatism. Ideally, the illumination of the sample should be parallel. Tilted illumination introduces higher ellipticity of Thon rings due to the higher-order aberrations [26]. In this work, we assume that CTF modulation is space-invariant over the entire micrograph. This is valid for most HREM and single particle EM studies in which the grid plane is perpendicular to the parallel incident electron beam. The astigmatism is usually constant for a sequential data collection, whereas the defocus is likely to show larger variation, in particular for tomography. Therefore, it is advisable to accurately measure astigmatism on a zero-tilt diffractogram, correct for the astigmatism if required, and then continue with image acquisition. Defoci in tomograms can be measured using procedures described in [50,51].

Whereas algorithms that base their defocus estimation on 1D averaged PSD are sensitive to sample drift and missing rings in the PSD, our algorithm based on template matching proved to be robust (see e.g. Fig. 14A and B). The rings are successfully mapped

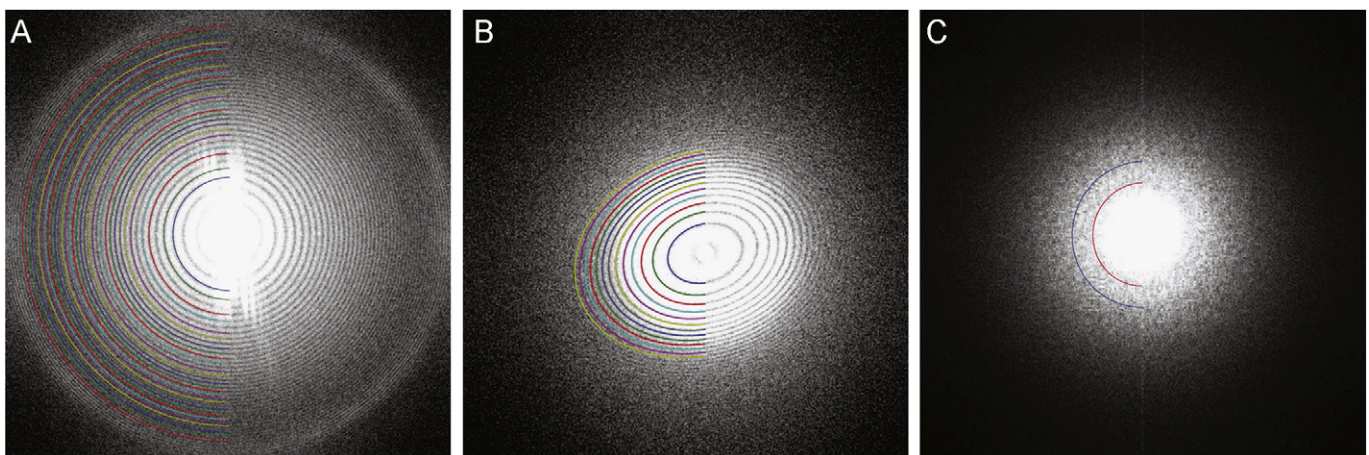


Fig. 14. (A) PSD of an image (size $4k \times 4k$ pixels) acquired on a Titan equipped with an X-FEG electron gun. The disturbance probably comes from specimen drift. Estimated defocus 1120 ± 2 nm; estimated astigmatism 1.6 ± 0.1 nm; Magnification 155 kx; (B) PSD of an image (size $4k \times 4k$ pixels) acquired on a Tecnai F20 (with a FEG electron gun). Estimated defocus 969 ± 13 nm; estimated astigmatism 269 ± 3 nm; magnification 62 kx. (C) PSD of an image (size 1536×1536 pixels) of hemoglobin embedded in vitreous ice acquired on a Tecnai T12 equipped with a LaB₆ electron gun. The image was taken with an incident electron flux of $\sim 5 \text{ e}^-/\text{\AA}^2$ at the edge of a hole of a Cflat support film and includes $\sim 30\%$ of the support. Estimated defocus 4521 ± 444 nm; estimated astigmatism 166 ± 50 nm; Magnification 50 kx. The calculated Thon rings are mapped only over the angular range of 180° for better comparison. For the display a percentile stretch was used (the lower and upper 1% of the gray values were clipped before stretching).

even when their completeness is compromised by external disturbance. Estimation from images with larger astigmatism values is still possible, although the rings can be incomplete (see Fig. 14B), due to the fact that the spatial envelope Eq. (7) dampens the contrast of the rings in one direction more than in another. Although such bad images could be discarded, we can still use them for defocus and astigmatism estimation illustrating the robustness of our technique.

The method takes the C_s influence into account and thus can be used on all microscopes (with or without C_s corrector). The algorithm's accuracy increases with the number of rings (see Table 2). Consequently, it might be beneficial to first estimate and correct astigmatism using higher magnification and then go back to the desired magnification. If only one or a few Thon rings are visible, it might also be advantageous to use an alternative pre-processing strategy that relies on bilateral filtering [52,53] and provides a better segmentation of low-frequency rings. This option is included in the provided software implementation of our algorithm. Furthermore, the spatial (and/or tonal) blurring of the adaptive and/or bilateral filter could be modified to make the rings more prominent. An example of defocus and astigmatism estimation from the PSD with barely visible Thon ring is shown in Fig. 14C.

Most of the algorithms developed so far (including ours) base their defocus estimation on the frequency of one or more minima in the PSD. This becomes quite a challenging task when the specimen is embedded in vitreous ice due to extremely low SNR. Alternatively to the PSD, some other measures can be used as the input for our algorithm, such as differential phase residual [54,55] or figure of merit [56–58]. These measures, however, rely on more than one acquisition. A remaining challenge is to accurately estimate the defocus at each location of the (non)tilted specimens embedded in vitreous ice, especially if no amorphous carbon is present in the image.

The set of presented algorithms have been implemented in MATLAB and are available as a part of the image-processing toolbox DIPimage (<http://www.diplib.org>). Some of the possible applications of the algorithm are described in [59].

Acknowledgments

The authors would like to thank Bram Koster for useful discussions, Pieter Brandt for help on the k -trajectory method and Remco Schoenmakers for critical reading of the manuscript. M. Vulović was financially supported by the FOM Industrial Partnership program No. 07.0599. RBGR acknowledges financial support from NWO under project number 016.072.321.

Appendix A. Weak-phase weak-amplitude approximation

Assuming an incident plane wave $\Psi_{\text{in}}(x,y) = 1$, a weak potential (both the real and imaginary part of $v_z(x,y)$ in Eq. (10)), and applying the first order Taylor expansion, the exit wave from the specimen can be written as

$$\Psi_{\text{ex}}(x,y) = e^{i\sigma v_z(x,y)} \approx 1 + i\sigma V_z(x,y) - \sigma \Lambda_z(x,y). \quad (\text{A.1})$$

The Fourier transform of the exit wave is then

$$\tilde{\Psi}_{\text{ex}}(q) = \delta(q) + i\sigma \tilde{V}_z(q) - \sigma \tilde{\Lambda}_z(q). \quad (\text{A.2})$$

Without loss of generality let us assume no astigmatism is present (i.e. $T(q,\alpha) = T(q)$). Substituting Eq. (3) in Eq. (4) we obtain

$$\begin{aligned} \tilde{\Psi}_{\text{im}}(q) &= \tilde{\Psi}_{\text{ex}}(q) K_a(q) e^{-i\chi(q)} \\ &= \tilde{\Psi}_{\text{ex}}(q) K_a(q) [\cos(\chi(q)) - i \sin(\chi(q))], \end{aligned} \quad (\text{A.3})$$

where $K_a(q) = K(q)A_p(q)$. $K(q)$ and $A_p(q)$ are defined in Eqs. (8) and (9) respectively. The Fourier transform of the image intensity can be written as

$$\tilde{I}(q) = \mathcal{F}[|\Psi_{\text{im}}(x,y)|^2] = \tilde{\Psi}_{\text{im}}^*(-q) * \tilde{\Psi}_{\text{im}}(q). \quad (\text{A.4})$$

For point-symmetric aberrations such as defocus, astigmatism and spherical aberration it holds that $\chi(-q) = \chi(q)$. Considering that $V_z(x,y)$ and $\Lambda_z(x,y)$ are real we have $\tilde{V}_z^*(-q) = \tilde{V}_z(q)$ and $\tilde{\Lambda}_z^*(-q) = \tilde{\Lambda}_z(q)$ and therefore

$$\begin{aligned} \tilde{I}(q) &= \int_{-\infty}^{\infty} (\delta(q') - i\sigma \tilde{V}_z(q') - \sigma \tilde{\Lambda}_z(q')) \\ &\quad \times K_a(q') [\cos(\chi(q')) + i \sin(\chi(q'))] \\ &\quad \times (\delta(q-q') + i\sigma \tilde{V}_z(q-q') - \sigma \tilde{\Lambda}_z(q-q')) \\ &\quad \times K_a(q-q') [\cos(\chi(q-q')) - i \sin(\chi(q-q'))] dq'. \end{aligned} \quad (\text{A.5})$$

Since $\sigma \tilde{V}_z(q) \ll \delta(q)$ and $\sigma \tilde{\Lambda}_z(q) \ll \delta(q)$ we can neglect the second order terms in q and the convolution reduces to

$$\tilde{I}(q) = \delta(q) + 2K_a(q)\sigma [\tilde{V}_z(q) \sin(\chi(q)) - \tilde{\Lambda}_z(q) \cos(\chi(q))]. \quad (\text{A.6})$$

Since

$$\begin{aligned} a \sin(x) - b \cos(x) \\ = \text{sgn}(a) \sqrt{a^2 + b^2} \sin\left(x - \arcsin\left(\frac{b}{\sqrt{a^2 + b^2}}\right)\right), \end{aligned} \quad (\text{A.7})$$

Eq. (A.6) can be rewritten as

$$\begin{aligned} \tilde{I}(q) &= \delta(q) + \text{sgn}(\tilde{V}_z(q)) \sigma \sqrt{\tilde{V}_z(q)^2 + \tilde{\Lambda}_z(q)^2} \\ &\quad 2K_a(q) \sin(\chi(q) - \arcsin(W(q))), \end{aligned} \quad (\text{A.8})$$

where $W(q)$ is the amount of the amplitude contrast as defined in Eq. (11). Since $W(q)$ for thin amorphous carbon (PtIr) is typically $\sim 6-10\%$ [46], $\sqrt{\tilde{V}_z(q)^2 + \tilde{\Lambda}_z(q)^2} \approx |\tilde{V}_z(q)|$ and the final intensity can be expressed as

$$\tilde{I}(q) = \delta(q) + \sigma \tilde{V}_z(q) 2K_a(q) \sin(\chi(q) - \arcsin(W(q))). \quad (\text{A.9})$$

Appendix B. Templates

B.1. Derivation of the template ellipticity R_t

The central frequency of each generated template is in the middle of the frequency range (i.e. $q_{ct} = N/4$). For simplicity and without loss of generality, let the generated templates have $\alpha_1 = \pi/4$. From Eqs. (22) and (30) the frequencies of the long and short axis can be expressed as

$$q_l = \sqrt{\frac{q_c^2(R_0^2 + 1)}{2}}, \quad (\text{B.1a})$$

$$q_s = \sqrt{\frac{q_c^2(R_0^2 + 1)}{2R_0^2}}. \quad (\text{B.1b})$$

From step 4 in Fig. 3, the peak-to-peak amplitude of the curve can be expressed as

$$A = q_l - q_s = q_s(R_0 - 1) = q_c(R_0 - 1) \sqrt{\frac{R_0^2 + 1}{2R_0^2}}. \quad (\text{B.2})$$

Templates match when the peak-to-peak amplitudes of the template and the pattern in the polar image are the same, i.e. $A_t = A_p$

$$(R_t - 1) \sqrt{\frac{R_t^2 + 1}{2R_t^2}} q_{ct} = (R_0 - 1) \sqrt{\frac{R_0^2 + 1}{2R_0^2}} q_c,$$

$$(R_t - 1)^2 (R_t^2 + 1) = 2cR_t^2 q_c^2,$$

where

$$c = \frac{R_0 - 1}{q_{ct}} \sqrt{\frac{R_0^2 + 1}{2R_0^2}}$$

is constant. The solution that has physical meaning ($R_t \in \mathbb{R}^+$) gives the relation between the template ellipticity and the central frequency:

$$R_t(q_c) = \frac{1}{2} + \frac{1}{2} \sqrt{2c^2 q_c^2 + 1} + \frac{1}{\sqrt{2}} \left[\sqrt{2c^2 q_c^2 + 1} + c^2 q_c^2 - 1 \right]^{1/2} \quad (\text{B.3})$$

B.2. The difference between detected q_{found} and central frequency q_c

Combining Eqs. (22) and (26) yields the polar representation of an ellipse

$$C(\alpha) = \frac{q_l}{\sqrt{\cos^2 \alpha + (R_0 \sin \alpha)^2}}. \quad (\text{B.4})$$

Its mean value is

$$q_m(R_t) = \langle C(\alpha) \rangle_\alpha = \frac{q_l}{\pi} I_{\text{el}}(R_t), \quad (\text{B.5})$$

where

$$I_{\text{el}}(R_t) = \int_0^\pi \frac{d\theta}{\sqrt{1 + (R_t^2 - 1) \sin^2 \theta}} \quad (\text{B.6})$$

is the incomplete elliptic integral of the first kind. Since the maxima in the parameter space provide also R_t we can use it to numerically solve the integral $I_{\text{el}}(R_t)$. Using Eq. (B.1a) the relative error between the mean (Eq. (B.5)) and central frequency of Eq. (B.4) is

$$\varepsilon_{R_t} = \frac{q_m - q_c}{q_m} = \frac{\sqrt{1 + R_t^2} I_{\text{el}}(R_t) - \sqrt{2}\pi}{\sqrt{1 + R_t^2} I_{\text{el}}(R_t)}. \quad (\text{B.7})$$

The response of the template matching depends on the difference between the mean value of the polar transformed Thon ring q_m and the mean value of the generated template $q_{m,t}$. Since central frequencies of the templates are fixed to $N/4$, the mean values $q_{m,t}$ are slightly shifted and that indicates that

$$q_{\text{found}}(R_t) = q_m - q_{m,t} + \frac{N}{4}. \quad (\text{B.8})$$

The central frequency that is needed for defocus and astigmatism estimation is

$$q_c = q_m(1 - \varepsilon_{R_t}). \quad (\text{B.9})$$

From Eqs. (B.8) and (B.9) we can write

$$q_{\text{found}}(R_t) = \frac{q_c - \frac{N}{4}}{1 - \varepsilon_{R_t}} + \frac{N}{4}. \quad (\text{B.10})$$

Thus the central frequency as a function of the found response in parameter space is

$$q_c = \left(q_{\text{found}} - \frac{N}{4} \right) (1 - \varepsilon_{R_t}) + \frac{N}{4}. \quad (\text{B.11})$$

Appendix C. Thon ring outlier rejection

From the collection of possible Thon ring candidates \mathcal{C} ordered by frequency q we calculate a list of selected Thon rings \mathcal{S} given by

$$\mathcal{S} = \{(q_1, s_1), (q_2, s_2), \dots, (q_N, s_N)\}, \quad (\text{C.1})$$

where \mathcal{S} is a subset of \mathcal{C} with an extra element s_i added to the tuple, which specifies how many Thon rings are skipped between the selected Thon ring i and $i-1$.

Outlier rejection restricts the number of possible subsets \mathcal{S} by the following restrictions:

$$\forall_i : \left| \frac{q_i^2 - q_{i-1}^2}{s_i \cdot d_i} \right| \leq \text{maxRelativeError} \quad (\text{C.2})$$

and

$$\sum_{i=1}^N s_i \leq \text{maxThonRingsSkip} \quad (\text{C.3})$$

where d_i represents the expected q^2 -distance between Thon rings $i-1$ and i , which is recursively defined as

$$d_{i+1} = \frac{1}{2} \left(\frac{q_i^2 - q_{i-1}^2}{s_i} + d_i \right), \quad (\text{C.4})$$

$$d_1 = \text{median}(q_i^2 - q_{i-1}^2). \quad (\text{C.5})$$

By default our implementation allows an error of equidistance of 20% ($\text{maxRelativeError}=0.2$) and the maximal number of skipped Thon rings is set to $\text{maxThonRingsSkip}=6$. The reason for the recursive definition in Eq. (C.4) is that we get an IIR-filter-like refinement of the q^2 -distance between Thon rings as we increase q , which is desirable as in fact the distance is not truly constant for $C_s \neq 0$. Furthermore, the distance also changes in the presence of amplitude contrast.

Appendix D. Spherical aberration influence

D.1. C_s influence on the ellipticity

Thon ring frequencies in the PSD correspond to the zeros of the CTF ($\chi(q, \alpha) = k_{\text{eff}} \pi$). The frequencies of the Thon rings in long/short axis orientation can be found from

$$\frac{C_s \lambda^3}{2} q_{l,s}^4 - \Delta f_{l,s} \lambda q_{l,s}^2 - k_{\text{eff}} = 0. \quad (\text{D.1})$$

It follows that

$$q_{l,s}^2 = \frac{\Delta f_{l,s} \pm \sqrt{\Delta f_{l,s}^2 + 2C_s k_{\text{eff}}}}{C_s \lambda^2}. \quad (\text{D.2})$$

For weak-amplitude samples $k_{\text{eff}} \approx k$ holds. The apparent ellipticity of the ring i is then

$$Q_i^2(k) = \frac{\Delta f_s \pm \sqrt{\Delta f_s^2 + 2C_s k}}{\Delta f_l \pm \sqrt{\Delta f_l^2 + 2C_s k}}, \quad (\text{D.3})$$

where i is the order of CTF zero for corresponding k -value. Since $Q_i^2(k) > 1$, we keep $-\sqrt{\Delta f_{l,s}^2 + 2C_s k_{\text{eff}}}$ for overfocus ($\Delta f < 0$, $A_1 < 0$ and $k \in \mathbb{N}$), and $+\sqrt{\Delta f_{l,s}^2 + 2C_s k_{\text{eff}}}$ for underfocus ($k \in \mathbb{Z}$ and $|k| \leq N_{0 \text{ max}}$). Eq. (D.3) can be written as

$$Q_i(k) = \sqrt{\frac{|\Delta f_s| + \sqrt{\Delta f_s^2 + 2C_s k}}{|\Delta f_l| + \sqrt{\Delta f_l^2 + 2C_s k}}} \quad (\text{35})$$

and its solutions are real and Thon rings are elliptic-like as long as

$$k \geq -\frac{\Delta f_l^2}{2C_s \lambda}. \quad (\text{D.4})$$

From Eq. (1) it is expected that the ellipticity of the rings decreases with frequency due to the influence of C_s which is angularly symmetric. Similarly, by increasing C_s , the apparent

ellipticity at a certain frequency should decrease (note, however, that changes in C_s are less influential than changes in q in Eq. (1)). This is directly visible in overfocus where ellipticity decreases monotonically with frequency and/or C_s . In underfocus, however, initially it increases after which it decreases. If the initial increase (in underfocus) is large, the condition Eq. (D.4) might not be satisfied, implying the formation of the rings that are no more elliptic-like but rather hyperbolic-like.

D.2. C_s influence on CTF minima position $q_{c,i}$

For the case $C_s = 0$, the neighboring CTF minima in squared frequency space are equidistant:

$$\Delta q_{c,i}^2|_{C_s=0} = \frac{\Delta k_i}{-\lambda \Delta f},$$

$$\text{with } |\Delta k_i| \equiv |k_{i+1} - k_i| = 1. \quad (\text{D.5})$$

When C_s cannot be neglected, the position of the CTF minima can be found from

$$\frac{C_s \lambda^3}{2} q_c^4 - \lambda \Delta f q_c^2 = k,$$

$$\frac{C_s \lambda^3}{2} (q_{c,i+1}^4 - q_{c,i}^4) - \lambda \Delta f (q_{c,i+1}^2 - q_{c,i}^2) = \Delta k_i.$$

The distance between neighboring minima in squared frequency space is now

$$\Delta q_{c,i}^2|_{C_s \neq 0} = \frac{\Delta k_i}{-\lambda \Delta f + \frac{C_s \lambda^3}{2} (q_{c,i+1}^2 + q_{c,i}^2)}. \quad (\text{D.6})$$

If β is the fraction of the C_s influence defined in Eq. (33) then we have

$$q^2 = \frac{2\beta |\Delta f|}{C_s \lambda^2}. \quad (\text{D.7})$$

Substituting Eq. (D.7) in Eq. (D.6) we obtain

$$\Delta q_{c,i}^2|_{C_s \neq 0} = \frac{\Delta k_i}{-\lambda \Delta f + \lambda \Delta f (\beta_{i+1} + \beta_i)}. \quad (\text{D.8})$$

The relative error between equidistant CTF zeros ($C_s = 0$) and distances when $C_s \neq 0$ can be presented as

$$\varepsilon_{C_s} = \frac{\Delta q_{c,i}^2|_{C_s \neq 0} - \Delta q_{c,i}^2|_{C_s = 0}}{\Delta q_{c,i}^2|_{C_s = 0}} = \frac{1}{1 - (\beta_{i+1} + \beta_i)} - 1. \quad (\text{D.9})$$

For example if $\beta_i \approx 10\%$ then $\varepsilon_{C_s} = 25\%$.

D.3. Correction for the C_s influence on the ring ellipticities

When $C_s > 0$, the Thon ring ellipses (that is, approximate ellipses), do not all have the same ellipticity. Therefore, we have to make a clear distinction in ellipticity of an individual Thon ring ellipse, which we will call Q_i for Thon ring i , given by

$$Q_i = \frac{q_{li}}{q_{s,i}}, \quad (\text{34})$$

where the long axis in the PSD is given by frequency q_{li} and short axis by $q_{s,i}$. We will keep on using the symbol R_0 as the dimensionless measure of astigmatism given by

$$R_0 = \sqrt{\frac{\Delta f + A_1}{\Delta f - A_1}}. \quad (\text{21})$$

Note that $Q_i|_{C_s=0} = R_0$ for all Thon rings. For $C_s > 0$, however, we detect Q_i for each Thon ring, but how to find the equivalent ellipticity R_{eq} for all rings? To obtain this relation, we define the

frequency q_v that is equivalent to the frequency q if C_s would be zero. That is, their phases and k -values in Eq. (1) are equal.

$$\frac{1}{2} C_s \lambda^3 q^4 - \lambda q^2 \Delta f = -\lambda q_v^2 \Delta f. \quad (\text{D.10})$$

Solving for q_v^2 yields

$$q_v^2 = \frac{q^2 \Delta f - \frac{1}{2} C_s \lambda^2 q^4}{\Delta f}. \quad (\text{D.11})$$

The frequency q_v is always real in overfocus. However, in underfocus the additional relation $2|\Delta f|/C_s \lambda^2 q^2 > 1$ must be fulfilled. If we use Eq. (D.11) to get values q_{vl} and q_{vs} for long and short axes, we recalculate R_{eq} by using

$$R_{eq}^2 = \frac{q_{vl}^2}{q_{vs}^2} = \frac{(2\Delta f_l q_l^2 - C_s \lambda^2 q_l^4) \Delta f_s}{(2\Delta f_s q_s^2 - C_s \lambda^2 q_s^4) \Delta f_l}. \quad (\text{D.12})$$

The numerator and denominator of the first fraction in the right-hand-side term are equal to k and the whole first fraction is equal to one. Thus, $R_{eq} = R_0$ equivalent ellipticity is equal to the ellipticity when $C_s = 0$. The problem is that we do not know this R_0 . R_{eq} can be further rewritten as

$$R_{eq} = R_0 \sqrt{\frac{q_{li}^2}{q_{s,i}^2} \frac{(2\Delta f_l - C_s \lambda^2 q_{li}^2)}{(2\Delta f_s - C_s \lambda^2 q_{s,i}^2)}}. \quad (\text{D.13})$$

From the first estimate (up to $\beta = 10\%$) we get initial values for R_0 , Δf_l and Δf_s . Furthermore, we refine the estimate by finding Q_i from the whole spectrum. These values are scaled with the second fraction in Eq. (D.13) and in this way the final R_{eq} is obtained.

Appendix E. Thon ring averaging

This section describes our new method for obtaining 1D profiles from the PSD of a micrograph. The most basic method used to obtain such a 1D profile is circular averaging, calculated using the discretized form (i.e. integration becomes summation) of the following equation:

$$p(q) = \frac{1}{\pi} \int_0^\pi d\alpha \int_{-3\sigma(q)}^{+3\sigma(q)} P(q+q', \alpha) G_{\sigma(q)}(q') dq'. \quad (\text{E.1})$$

where G_σ is a Gaussian kernel of scale σ , which can be a function of the radial frequency q . Some blurring with the Gaussian is applied to ensure smooth results on the discretized power spectrum. The sum over q' is bound to an interval of e.g. $-3\sigma, +3\sigma$ to make the implementation efficient but also approximate the Gaussian accurately. Circular averaging only exactly follows the Thon rings when there is no astigmatism. With astigmatism, one should use elliptical averaging, defined as

$$p_{R,\alpha_1}(q) = \frac{1}{\pi} \int_0^\pi d\alpha \int_{-3\sigma(q)}^{+3\sigma(q)} P(q', \alpha) G_{\sigma(q)}(q') dq',$$

$$P(q', \alpha) = P\left(\frac{q+q'}{\sqrt{1+(R^2-1)\sin^2(\alpha-\alpha_1)}}, \alpha\right), \quad (\text{E.2})$$

where ellipticity R and α_1 represent the astigmatism influence.

When $C_s \neq 0$, Thon rings start to deviate from ellipses. With Thon ring averaging, we aim at getting averages over Thon rings as function of their central frequencies q_c . To correctly average over Thon rings we consider Eq. (1). Using this equation, we can find the “nominal radius” q_c of any position in the PSD (so not only frequencies of the Thon rings) by equating the latter formula

to the same formula without the astigmatism term:

$$\frac{1}{2}C_s\lambda^3q^4 - \lambda q^2(\Delta f - A_1 \cos(2(\alpha - \alpha_1))) = \frac{1}{2}C_s\lambda^3q_c^4 - \lambda q_c^2\Delta f. \quad (\text{E.3})$$

Solving for q_c^2 we find

$$q_c^2 = \frac{\Delta f \pm \sqrt{\Delta f^2 + 2C_s\lambda k}}{C_s\lambda^2}. \quad (\text{E.4})$$

where $k = \frac{1}{2}C_s\lambda^3q^4 + \lambda q^2(\Delta f - A_1 \cos(2(\alpha - \alpha_1)))$. The “ \pm ” sign in Eq. (E.4) is plus for overfocus and for monotonic increase of k values in underfocus, and minus when k values in underfocus monotonically decrease. The implementation of Thon ring averaging works as follows:

1. Create two empty 1D arrays `result` and `sum` of size $N/2$ and initialize with zeroes.
2. For each power spectrum position (q_x, q_y) :
 - (a) Convert coordinates (q_x, q_y) to polar coordinates (q, α) and calculate the corresponding q_c using Eq. (E.4)
 - (b) Add the Gaussian weighted response $G(q' - q_c)P(q, \alpha)$ to `result` by adding its value to the bins in the interval $[q_c - 3\sigma, q_c + 3\sigma]$.
 - (c) Add the responses of the Gaussian weight in the corresponding bin of the array `sum`.
3. Divide all elements of `result` componentwise by the elements of `sum`. Return `result`.

References

- [1] H.P. Erickson, A. Klug, Measurement and compensation of defocusing and aberrations by Fourier processing of electron micrographs, *Philosophical Transactions of the Royal Society of London, Series B* 261 (105) (1971) 105–118.
- [2] F. Thon, Phase contrast electron microscopy, *Electron Microscopy in Materials Science* (1971) 570–625.
- [3] A.J. Koster, A. van den Bos, K. van der Mast, An autofocus method for a TEM, *Ultramicroscopy* 21 (3) (1987) 209–222.
- [4] Z.H. Zhou, S. Hardt, B. Wang, M.B. Sherman, J. Jakana, W. Chiu, CTF determination of images of ice-embedded single particles using a graphics interface, *Journal of Structural Biology* 116 (1) (1996) 216–222.
- [5] M. van Heel, G. Harauz, E.V. Orlova, R. Schmidt, M. Schatz, A new generation of the IMAGIC image processing system, *Journal of Structural Biology* 116 (1) (1996) 17–24.
- [6] T.R. Shaikh, H. Gao, W.T. Baxter, F.J. Asturias, N. Boisset, A. Leith, J. Frank, SPIDER image processing for single-particle reconstruction of biological macromolecules from electron micrographs, *Nature Protocols* 3 (12) (2008) 1941–1974.
- [7] J.J. Fernández, J.R. Sanjurjo, J.M. Carazo, A spectral estimation approach to contrast transfer function detection in electron microscopy, *Ultramicroscopy* 68 (4) (1997) 267–295.
- [8] J. Zhu, P.A. Penczek, R. Schröder, J. Frank, Three-dimensional reconstruction with contrast transfer function correction from energy-filtered cryoelectron micrographs: procedure and application to the 70S *Escherichia coli* ribosome, *Journal of Structural Biology* 118 (3) (1997) 197–219.
- [9] J.F. Conway, A.C. Steven, Methods for reconstructing density maps of “single” particles from cryoelectron micrographs to subnanometer resolution, *Journal of Structural Biology* 128 (1) (1999) 106–118.
- [10] S.J. Ludtke, P.R. Baldwin, W. Chiu, EMAN: semiautomated software for high-resolution single-particle reconstructions, *Journal of Structural Biology* 128 (1) (1999) 82–97.
- [11] A. Saad, S.J. Ludtke, J. Jakana, F.J. Rixon, H. Tsuruta, W. Chiu, Fourier amplitude decay of electron cryomicroscopic images of single particles and effects on structure determination, *Journal of Structural Biology* 133 (1) (2001) 32–42.
- [12] J.A. Mindell, N. Grigorieff, Accurate determination of local defocus and specimen tilt in electron microscopy, *Journal of Structural Biology* 142 (3) (2003) 334–347.
- [13] B. Sander, M.M. Golas, H. Stark, Automatic CTF correction for single particles based upon multivariate statistical analysis of individual power spectra, *Journal of Structural Biology* 142 (3) (2003) 392–401.
- [14] J.A. Velázquez-Muriel, C.O.S. Sorzano, J.J. Fernández, J.M. Carazo, A method for estimating the CTF in electron microscopy based on ARMA models and parameter adjustment, *Ultramicroscopy* 96 (1) (2003) 17–35.
- [15] Z. Huang, P.R. Baldwin, S. Mullapudi, P.A. Penczek, Automated determination of parameters describing power spectra of micrograph images in electron microscopy, *Journal of Structural Biology* 144 (1–2) (2003) 79–94.
- [16] C.O.S. Sorzano, R. Marabini, J. Velázquez-Muriel, J.R. Bilbao-Castro, S.H.W. Scheres, J.M. Carazo, A. Pascual-Montano, XMIPP: a new generation of an open-source image processing package for electron microscopy, *Journal of Structural Biology* 148 (2) (2004) 194–204.
- [17] S.P. Mallick, B. Carragher, C.S. Potter, D.J. Kriegman, ACE: automated CTF estimation, *Ultramicroscopy* 104 (1) (2005) 8–29.
- [18] C.O.S. Sorzano, S. Jonic, R. Nez-Ramrez, N. Boisset, J.M. Carazo, Fast, robust, and accurate determination of transmission electron microscopy contrast transfer function, *Journal of Structural Biology* 160 (2) (2007) 249–262.
- [19] G. Tang, L. Peng, P.R. Baldwin, D.S. Mann, W. Jiang, I. Rees, S.J. Ludtke, EMAN2: an extensible image processing suite for electron microscopy, *Journal of Structural Biology* 157 (1) (2007) 38–46.
- [20] C. Yang, W. Jiang, D.H. Chen, U. Adiga, E.G. Ng, W. Chiu, Estimating contrast transfer function and associated parameters by constrained non-linear optimization, *Journal of Microscopy* 233 (3) (2009) 391–403.
- [21] K. Tani, H. Sasabe, C. Toyoshima, A set of computer programs for determining defocus and astigmatism in electron images, *Ultramicroscopy* 65 (1–2) (1996) 31–44.
- [22] K.V. Fernando, Radial averages of astigmatic TEM images, *Journal of Structural Biology* 164 (1) (2008) 49–59.
- [23] J. Barthel, A. Thust, Aberration measurement in HRTEM: implementation and diagnostic use of numerical procedures for the highly precise recognition of diffractogram patterns, *Ultramicroscopy* 111 (1) (2010) 27–46.
- [24] C.O. Sorzano, A. Otero, E.M. Olmos, J.M. Carazo, Error analysis in the determination of the electron microscopical contrast transfer function parameters from experimental power spectra, *BMC Structural Biology* 9 (2009) 18.
- [25] M. Vulovic, P. Brandt, R.B.G. Ravelli, A.J. Koster, L.J. van Vliet, B. Rieger, Estimation of defocus and astigmatism in transmission electron microscopy, in: *Proceedings of the IEEE International Symposium on Biomedical Imaging*, 2010, pp. 1121–1124.
- [26] F. Zemlin, K. Weiss, P. Schiske, W. Kunath, K.-H. Herrmann, Coma-free alignment of high resolution electron microscopes with the aid of optical diffractograms, *Ultramicroscopy* 3 (1978) 49–60.
- [27] A. Thust, C. Jia, K. Urban, Direct determination of imaging parameters from wave functions in HRTEM, *Microscopy and Microanalysis* 9 (2003) 140–141.
- [28] R. Meyer, A. Kirkland, W. Saxton, A new method for the determination of the wave aberration function for high resolution TEM 1. Measurement of the symmetric aberrations, *Ultramicroscopy* 92 (2002) 89–109.
- [29] A. Steinecker, W. Mader, Measurement of lens aberrations by means of image displacements in beam-tilt series, *Ultramicroscopy* 81 (2000) 149–161.
- [30] S. Uhlemann, M. Haider, Residual wave aberrations in the first spherical aberration corrected transmission electron microscope, *Ultramicroscopy* 72 (1998) 109–119.
- [31] A. Kirkland, W. Saxton, R. Meyer, Super resolved microscopy and aberration determination in the TEM, in: *Electron Microscopy and Analysis Group Conference EMAG97*, Cambridge, UK, 1997, pp. 105–108.
- [32] L. Reimer, H. Kohl, *Transmission Electron Microscopy*, 5th ed., Springer-Verlag, Berlin, 2008.
- [33] J. Barthel, A. Thust, Quantification of the information limit of transmission electron microscopes, *Physical Review Letters* 101 (20) (2008) 2008011–2008014.
- [34] L.M. Voortman, S. Stallinga, R.H.M. Schoenmakers, L.J. van Vliet, B. Rieger, A fast algorithm for computing and correcting the CTF for tilted, thick specimens in TEM, *Ultramicroscopy* 111 (8) (2011) 1029–1036.
- [35] S. Jonic, C.O.S. Sorzano, M. Cotteville, E. Larquet, N. Boisset, A novel method for improvement of visualization of power spectra for sorting cryo-electron micrographs and their local areas, *Journal of Structural Biology* 157 (1) (2007) 156–167.
- [36] P. Bakker, L.J. van Vliet, P.W. Verbeek, Edge preserving orientation adaptive filtering, in: *Conference on Computer Vision and Pattern Recognition*, vol. 2, IEEE Computer Society Press, Los Alamitos, CA, USA, 1999, pp. 535–540.
- [37] J. van de Weijer, L.J. van Vliet, P.W. Verbeek, R. van Ginkel, Curvature estimation in oriented patterns using curvilinear models applied to gradient vector fields, *IEEE Transactions on Pattern Analysis and Machine Intelligence* 23 (9) (2001) 1035–1042.
- [38] T.P. Harrigan, R.W. Mann, Characterization of microstructural anisotropy in orthotropic materials using a second rank tensor, *Journal of Materials Science* 19 (1984) 761–767.
- [39] M. Kass, A. Witkin, Analyzing oriented patterns, *Computer Vision, Graphics and Image Processing* 37 (1987) 362–385.
- [40] W. Förstner, E. Gülch, A fast operator for detection and precise location of distinct points, corners and centres of circular features, in: *Proceedings of the ISPRS Conference on Fast Processing of Photogrammetric Data*, 1987, pp. 281–305.
- [41] P.W. Verbeek, L.J. van Vliet, On the location error of curved edges in low-pass filtered 2-D and 3-D images, *IEEE Transactions on Pattern Analysis and Machine Intelligence* 16 (7) (1994) 726–733.
- [42] C.L. Luengo Hendriks, M. van Ginkel, P.W. Verbeek, L.J. van Vliet, The generalized Radon transform: sampling, accuracy and memory considerations, *Pattern Recognition* 38 (12) (2005) 2494–2505.
- [43] G.C. Stockman, A.K. Agrawala, Equivalence of Hough curve detection to template matching, *Communications of the ACM* 20 (11) (1977) 820–822.

- [44] M. Vulovic, B. Rieger, L.J. van Vliet, A.J. Koster, R.B.G. Ravelli, A toolkit for the characterization of CCD cameras for transmission electron microscopy, *Acta Crystallographica Section D* 66 (1) (2010) 97–109.
- [45] R.F. Egerton, K. Wong, Some practical consequences of the Lorentzian angular distribution of inelastic scattering, *Ultramicroscopy* 59 (1–4) (1995) 169–180.
- [46] K. Yonekura, M. Braunfeld, S. Mari-Yonekura, D. Agard, Electron energy filtering significantly improves amplitude contrast of frozen-hydrated protein at 300 kV, *Journal of Structural Biology* 156 (3) (2006) 524–536.
- [47] S. Nickell, F. Förster, A. Linaroudis, W.D. Net, F. Beck, R. Hegerl, W. Baumeister, J.M. Plitzko, TOM software toolbox: acquisition and analysis for electron tomography, *Journal of Structural Biology* 149 (3) (2005) 227–234.
- [48] W. Saxton, W. Baumeister, The correlation averaging of a regularly arranged bacterial cell envelope protein, *Journal of Microscopy* 127 (2) (1982) 127–138.
- [49] B.A. Walther, J.L. Moore, The concepts of bias, precision and accuracy, and their use in testing the performance of species richness estimators, with a literature review of estimator performance, *Ecography* 28 (6) (2005) 815–829.
- [50] J.J. Fernández, S. Li, R.A. Crowther, CTF determination and correction in electron cryotomography, *Ultramicroscopy* 106 (7) (2006) 587–596.
- [51] Q. Xiong, M.K. Morpew, C.L. Schwartz, A.H. Hoenger, D.N. Mastronarde, CTF determination and correction for low dose tomographic tilt series, *Journal of Structural Biology* 168 (3) (2009) 378–387.
- [52] C. Tomasi, R. Manduchi, Bilateral filtering for gray and color images, in: *Sixth International Conference on Computer Vision*, 1998, pp. 839–846.
- [53] T.Q. Pham, L.J. van Vliet, Separable bilateral filtering for fast video preprocessing, in: *ICME 2005. IEEE International Conference on Multimedia and Expo*, 2005, p. 4.
- [54] J. Frank, A. Verschoor, M. Boublik, Computer averaging of electron micrographs of 40S ribosomal subunits, *Science* 214 (4527) (1981) 1353–1355.
- [55] M.V. Heel, Similarity measures between images, *Ultramicroscopy* 21 (1) (1987) 95–100.
- [56] M. Karuppasamy, F. Karimi Nejadasl, M. Vulovic, A.J. Koster, R.B.G. Ravelli, Radiation damage studies in single particle cryo-electron microscopy: effects of dose and dose rate, *Journal of Synchrotron Radiation* 18 (3) (2011) 398–412.
- [57] F.K. Nejadasl, M. Karuppasamy, A.J. Koster, R.B.G. Ravelli, Defocus estimation from stroboscopic cryo-electron microscopy data, *Ultramicroscopy* 111 (11) (2011) 1592–1598.
- [58] D.M. Blow, F.H.C. Crick, The treatment of errors in the isomorphous replacement method, *Acta Crystallographica* 12 (10) (1959) 794–802.
- [59] E. Franken, R. Wagner, R. Schoenmakers, M. Vulovic, Applications of accurate defocus and astigmatism estimation, in: *EMBL Conference: Sixth International Congress on Electron Tomography*, Heidelberg, Germany, 2011, p. 80.